Data assimilation

Andreas Schröder, Philipp Godbersen, Florian Huhn, Sebastian Gesemann, Daniel Schanz

DLR German Aerospace Center
Institute of Aerodynamics and Flow Technology

December 4th, 2024

Data assimilation (DA) emerged already in the 1950s in the field of weather prediction frame works, which involves the usage of sparse and limited measurement data in time series at discrete weather stations, based on which numerical predictions for future weather conditions can be supported (Navon 2009). With the rising computational capabilities over the past decades various DA schemes have been developed in the field of fluid mechanics and implemented by incorporating mathematical and numerical methods like ensemble Kalman filtering based or other variational approaches (4D- or 3DVar) mostly including adjoint CFD schemes or fully DNS/LES based adjoint methods, continuous and grid-based augmentation and interpolation using physical constraints and Physics Informed Neural-Networks (PINN's). Another field of DA is lower order modelling and filtering of PIV and PTV data using (gappy) POD, LSE or DMD methods, which can serve as basis for "super-resolution" approaches. All these methods gained increasing interest in the past couple of years and demonstrated their possibilities within applications to a wide field of inverse problems based on probe, 2D- or full 3D-flow field measurement data (Agarwal et al 2021, Appelbaum et al 2021, Beneddine et al 2017, Buchta et al 2022, Cai et al 2023, Cakir et al 2023, Chandramouli et al 2020, Clark di Leonie et al 2023, Discetti and Liu 2022, Du et al. 2023, Duraisamy 2019, Ehlers et al 2020, Fukami et al 2021, Gesemann et al 2016, Godbersen et al 2024, Gronskis et al 2013, Hanrahan et al 2023, He et al 2022, He et al 2024, Jeon et al. 2022, Lemke and Sesterhenn 2016, Leoni et al 2023, Li and Pan 2024, Mons et al 2022, Navon 2009, Raissi et al 2019/2020, Scarano et al 2022, Schneiders and Scarano 2016, Sperotto et al 2022, Suzuki et al 2009a/b, Suzuki and Yamamoto 2015, Van Gent et al 2017, Wang and Zaki 2021, Zauner et al 2022, Zhou and Grauer 2023, Zhou et al 2024).

In experimental fluid mechanics and aerodynamics 3D PIV and -LPT measurement techniques provide a well-suited input basis for such DA schemes. Especially, volumetric LPT data with temporal resolution can deliver position, velocity and acceleration (material derivative) vector information along a huge number of individual particle trajectories inside the measured fluid flow (today mainly by Shake-The-Box) for various data assimilation methods allowing for a high-resolution interpolation of the time-resolved 3D velocity-, velocity gradient tensor (VGT)- and pressure fields by using physical constraints (Navier-Stokes-equations). A two- or four-pulse 3D LPT system can at least provide position and velocity distributions in a scattered manner from which data assimilation schemes can derive significant instantaneous flow quantities (coherent structures, vorticity, Q-values etc) which are important for the understanding and characterization of the investigated flow field and validation of CFD

methods. The resolution and accuracy of the resulting flow field interpolation is limited by the measurement accuracy and the mean 3D inter-particle distances of the particle trajectories in terms of Kolmogorov length scales, but as well by the quality and performance of the used DA algorithm, which might involve physical laws, neural networks, adjoint methods or temporal information. Two recent studies show superior resolution and accuracies for 4D VAR methods over PINNs (Du et al 2023) and for PINNs over FlowFit and VIC# (Zhou et al 2024), but with significantly lower computational costs for the latter methods. Such synthetic and experimental benchmark tests, e.g. performed as an international challenge with an independent jury (Sciacchitano et al. 2021), are a welcome frame work for comparing and discussing implementation details of the various algorithms and for inspiring further developments. Furthermore, related publications and online accessible benchmark test platforms demonstrate the capabilities of the various DA algorithms in comparison to each other and in outperforming simple interpolation methods e.g. based on weighted binning or adaptive smoothing with polynomials or other functionals.

Already in the past, with grid based and low-pass filtered snapshot or time-resolved tomo-PIV or sparse PTV data many groups have developed methods that compute unsteady pressure fields (Fujisawa et al 2005, Liu and Katz 2006, Kurtulus et al 2007, Murai et al 2007, Suzuki et al 2009a, 2009b, Violato et al 2011, Oudheusden et al. 2013)

By solving the pressure -Poisson-equation 3D (or 2D) pressure fields can be estimated. The solvers are typically based on (time-series) of instantaneous PIV results and use certain assumptions, boundary conditions and various integration schemes, depending on the available flow data. For scattered 3D LPT results single time-step techniques for data assimilation schemes have been established using solenoidal constraints or a full incompressible Navier-Stokes-regularization. For the latter velocity and acceleration (material derivative) of the particle tracks are used as input values (left side of the momentum equation) for e.g. FlowFit, VIC +/# (Gesemann et al 2016, Godbersen et al 2024, Schneiders and Scarano 2016). Those schemes provide a continuous functional representation of the assimilated velocity vector field with-out additional spatial filtering (on the basis of (truncated) 3D radial basis functions of Gaussian shapes or B-Splines). Analytical derivatives can be computed for the VGT $A_{ij}(t)$ and 3D pressure fields are integrated by solving the Poisson equation implicitly using non-linear optimization solvers (e.g. L-BFGS). These methods can be improved by exploiting the available time-series of LPT data by using advection models with smoothness constraints for du/dt and dω/dt of the VGT (Jeon et al 2022), finite time-segments of particle trajectories (Scarano et al 2022) or advection of virtual particles from time-step to time-step (Ehlers et al 2020). A relatively new and fast developing field of DA based on 3D LPT data are physics-informed-neural networks (PINNs) (Raissi et al. 2019/2020) which fit a solution of the inverse augmentation problem along a full time-series of trajectories (> 10 time-steps) while penalizing deviations to the measurement data at particle positions (u_p and a_p), to continuity (div $u = 0$) and to the momentum equation. The augmentation results are generally smoother in space and time and have increased accuracies with respect to former and simpler methods (Zhou and Grauer 2023, Zhou et al. 2024), but on the other hand PINNs require training data inducing high computational costs (preferably on a GPU cluster).

Contents

1 Introduction and Motivation

Today, there are continuously increasing requirements for flow field investigations in aerodynamics and fluid mechanics research for both experimental and numerical methods: Flow configurations become more and more complex while the interest in unsteady and vortical flow phenomena in research and aeronautics industry is growing. For clarifying remaining theoretical aspects of turbulence, enhancing modelling and validation capabilities of advanced CFD codes at high Reynolds numbers experimental data describing the flow more completely and in whole fields or volumes are necessary.

3D PIV and LPT are able to provide unsteady as well as averaged velocity fields and related rms –values, vorticity etc. and have been developed to a reliable measurement tool in the recent years, but are still experimentally demanding for many applications in (large) test facilities (Scarano 2013, Discetti and Colletti 2018, Schröder and Schanz 2023). For gaining the time resolved 3D velocity gradient tensor and respective acceleration- and pressure fields at high accuracies and spatial resolution advanced 3D LPT and data assimilation methods are currently under development (Schanz et al. 2016a, Schanz et al. 2021, Schneiders et al. 2016, Gesemann et al. 2016).

Flow topologies can be defined either in a Eulerian (laboratory) reference system e.g. by the invariants Q and R of $A_{ij}(t)$ (for incompressible flows) (Chong et al. 1990) or from a Lagrangian perspective (Haller 2015, Haller et al. 2016) moving with the fluid elements. Furthermore, 3D pressure fields can be calculated e.g. directly via integration of the Poisson equation from time-resolved 3D velocity vector fields (van Oudheusden 2013, van Gent et al. 2017) or implicitly by data assimilation approaches using dense scattered Lagrangian velocity and acceleration vector fields as input (Gesemann et al. 2016, Huhn et al. 2018).

Most of the mathematical schemes to derive statistical values and spatial or temporal derivatives of independent and time-resolved x-dimensional vector fields can be found in respective books on mathematics and do not need to be written down here. For the part dealing with fluid mechanical values please look into Chong at al. 1990, Pope 2000, Chakraborty et al. 2005, Chakraborty et al. 2007, and specifically for PIV and LPT based data into Lourenco and Krothapalli 1995, Etebari and Vlachos 2005, Kurtulus et al. 2007, Adrian and Westerweel 2011, Ghaemi et al. 2012, van Oudheusden 2013, Novara and Scarano 2013, Kähler et al. 2016, Gesemann et al. 2016, Schneiders et al. 2016b, Schanz et al. 2016a, Raffel et al. 2018, and many others, partly by given by respective references.

In the remainder of this paper two recent developments in the frame of data assimilation are presented exemplarily: The recent development of FlowFit3 (Godbersen et al 2024) with its very efficient linear and non-linear modes is decribed and assessed in the first part. FlowFit3 is using LPT input data like its predecessor FlowFit2, either fully time-resolved or as short tracks (delivered by MP-STB, Novara et al. 2019)). Secondly, a specific approach using FlowFit 2 to achieve time-resolved 3D VGT and pressure fields from 3D LPT data in a large-scale impinging jet experiment using pulsed LED illumination of HFSB (Huhn et al. 2018) is enrolled and assessed with microphone measurements.

2 FlowFit3: Efficient data assimilation of LPT measurements

2.1 Introduction

3D Lagrangian particle tracking (LPT) (Schröder & Schanz, 2023) enables the accurate measurement of the position, velocity and acceleration of particles moving within fluid flows (Ouellette et al. 2006, Schanz et al. 2016a, Schröder and Schanz 2023). The scattered nature of the individually tracked particles provides a great advantage over other related measurement techniques such as PIV. Instead of a fixed regular grid of convolution windows, whose size imposes a low pass filtering effect on resolvable structures, particle positions are distributed in a stochastic manner and provide local point measurements. This can be exploited in Eulerian ensemble averaging using spatial binning to realize very fine resolutions, since the bin size is not directly linked to measurement technique and is primarily limited by the amount of available data. This allows a direct trade-off between bin size and convergence of the underlying statistic. One particularity of LPT is that we do not just have the position and velocity of a particle at each timestep but inherent to the processing a continuous track over a certain time range. This provides additional information as the single time steps are not independent but instead temporally linked.

Within this contribution we will focus on the Shake-The-Box (STB) approach for LPT where the two variants for time-resolved STB (Schanz et al. 2016a) and multi-pulse STB (Novara et al. 2019) express this temporal connection in slightly different ways. For time-resolved STB tracks can span up to the entire measurement duration directly providing significant temporal information. The multi-pulse variant necessary for faster flows provides temporal information only for the short bursts typically consisting of four pulses. This variant relies on collecting many bursts that are temporally uncorrelated from each other to build flow statistics. A small amount of temporal information is nevertheless available for each burst and within this paper we will mostly focus on the processing of such multi-pulse data. The presented approaches are generally not limited to multi-pulse STB but adaptable to any LPT measurement that provides access to this temporal data.

Often it is also desirable to have access to a grid-structured representation of the data, especially for the calculation of spatial gradients of flow field measures. While a simple interpolation onto a grid is possible, data assimilation techniques using physics-based regularization such as FlowFit2 (Gesemann et al. 2016) or VIC+ (Schneiders & Scarano 2016) and VIC# (Jeon et al. 2022) are frequently used nowadays. Through knowledge of the Navier-Stokes equations a higher spatial resolution can be obtained than from interpolation alone (see e.g. Zhou et al. 2024). We present the new and highly efficient FlowFit3 approach and its evaluation on synthetic data.

FlowFit3 is a new development within the existing FlowFit concept. Common to its predecessors is the representation of the instantaneous flow field using a 3D uniform B-spline grid of weighting coefficients. B-splines can be efficiently evaluated at arbitrary positions within the reconstructed volume and provide easy access to spatial gradients (see Figure 1). The FlowFit3 approach thoroughly changes the way these coefficients are determined from the data. In this paper we will focus on the description of the method and will conduct comparisons with prior FlowFit versions. A comprehensive evaluation of the results obtained using FlowFit3 in

comparison to other data assimilation techniques on synthetic and real-world data can be found in Zhou et al. (2024).

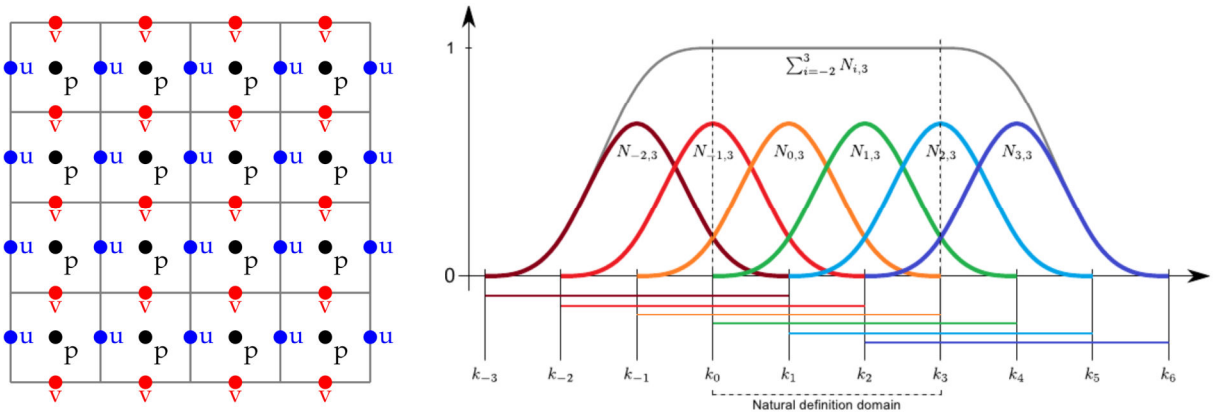

Figure 1: FlowFit3 basis: (left): Example of a 2D staggered grid. (right:) Example of 1D B-spline basis functions and interpolation. Lines at the bottom highlight the compact support

Just as with prior versions of FlowFit the incompressible Navier-Stokes equations are used as underlying physics equations:

$$\vec{a} = \vec{D}u/Dt = -\nabla\bar{p} + \nu\Delta\vec{u} \quad (1)$$

$$\nabla \cdot \vec{u} = 0 \quad (2)$$

In Figure 1 lines at the bottom highlight the limited support with velocity $\vec{u}$, acceleration $\vec{a}$, kinematic pressure $\bar{p}$ and kinematic viscosity ν. With LPT we directly measure the material derivative $\vec{D}u/Dt$ so there is no need to expand it into its convective form. By rearranging these equations, one also obtains an equation (3) for pressure which is used by some variants of FlowFit:

$$\Delta\bar{p} + \nabla \cdot ((\vec{u} \cdot \nabla)\vec{u}) = 0 \quad (3)$$

2.2 Method

We introduce two variants of FlowFit3, similar to the div1 and div2 modes of FlowFit2. The first, constraining the divergence of velocity (2), will be called "linear" mode in the following as only linear terms are involved in the physics constraint. No measured acceleration data is needed for this mode. The second variant is the "nonlinear" mode using also the momentum equation (1) as an additional constraint. This mode uses measured accelerations to improve the reconstruction and is also able to recover pressure fields using (3). Both modes build on the same internal architecture so we begin with an explanation of the simpler linear mode.

2.2.1 B-Spline representation

Just as in previous iterations of FlowFit a B-spline representation is used as basis for the data assimilation. This takes the form of a grid of spline basis functions of e.g. 3rd order, each with compact support. One can then select scaling weights for each of the basis functions. The

basis functions overlap, but due to the compact support only a small amount of basis functions is nonzero for a given point in the domain. In order to evaluate such a B-spline representation at a certain point, one needs to evaluate the value of all local basis functions at this position and scale them by their respective weighting coefficients. The sum now represents the evaluated value at that point.

The basis functions itself are fixed for a given FlowFit "grid" of continuous B-Splines so all that is needed during reconstruction is to compute appropriate weighting coefficients that best represent a given flow. Each of the components of the velocity vector (u,v,w) is considered a separate field. A finished FlowFit reconstruction corresponds to a grid of B-spline coefficients for each flow quantity which can be evaluated at arbitrary points within the domain. This setup also allows for easy evaluation of spatial gradients since the derivative of the spatial field can be obtained using the derivative of the basis functions which can be computed beforehand. In the following we will use the term coefficients to refer to the values of the B-spline coefficients themselves whereas the term field will be used for the resulting continuous interpolation (e.g, pressure coefficients vs. pressure field).

At its heart the data assimilation is accomplished by a gradient based optimization with a cost function that incorporates measured data as well as additional constraints. The measured data in the form of particles with positions and velocity values can simply be included by evaluating the current velocity field at the particles locations and examining the velocity difference, which is included as a term in the cost function. In order to move beyond simple interpolation knowledge of the underlying flow physics is included into the optimization. Assuming an incompressible fluid with constant density, the continuity equation transforms to a divergence constraint on the velocity field (2). Previous versions of FlowFit would incorporate such constraints as penalty terms into the cost function. Such a soft constraint has several disadvantages as not only this term has to be properly weighted with respect to the other cost function terms, the constraint is also not exactly enforced.

2.2.2 Hard constraint on divergence

One key improvement of FlowFit3 over prior versions is to move the divergence constraint into the design of the Ansatz instead. In this way the constraint is satisfied at any point in the domain and the optimizer is able to more efficiently reach an optimal solution as it is restricted from even considering infeasible solutions during intermediate steps. In the following we give a brief overview of how this is accomplished. FlowFit3 now utilizes a staggered grid (Harlow & Welch, 1965) for the velocity coefficients where the grids are shifted by half of the spacing. The shift is performed in the direction of the individual velocity component (e.g. in y-direction for v). A visual example of the resulting grid structure for the case of a 2D grid is given in Figure 1. In a 3D grid the w component is shifted similarly in the z-direction.

Such a staggered grid is useful to avoid the problem of even/odd decoupling when solving the pressure Possion equation which will be a topic when discussing the nonlinear mode. For the moment we will focus on the hard divergence constraint and how the staggered grid can be used for this. Originally such a grid was introduced for the application of finite differences used in the discretization of the spatial derivatives in the incompressible Navier-Stokes equations, but the concept applies to the use of uniform B-splines in a comparable way. The derivative of

an $(n+1)^{th}$ order uniform B-spline is an n-th order uniform B-spline on a grid shifted by half a spacing unit. The divergence of the velocity field requires the derivatives $\partial u/\partial x$, $\partial v/\partial y$ and $\partial w/\partial z$. If one constructs the 3D B-spline for u as (4th, 3rd, 3rd) order for (x, y, z) respectively then $\partial u/\partial x$ is a B-spline with (3rd, 3rd, 3rd) order. Moreover, since the derivative grid is shifted by half a spacing unit in the x-direction its location is now back at a grid position co-located with pressure. The same applies for the other staggered velocity components (e.g. (3rd, 4th, 3rd) order for v) giving a (3rd, 3rd, 3rd) order uniform B-spline for the divergence. If we wish to force this divergence to be zero everywhere the coefficients need to satisfy:

$$0 = (u_{x+1/2,y,z} - u_{x-1/2,y,z}) + (v_{x,y+1/2,z} - v_{x,y-1/2,z}) + (w_{x,y,z+1/2} - w_{x,y,z-1/2}) \quad (4)$$

Essentially the divergence of the coefficient grid needs to be zero, which then guarantees by construction that the divergence field is exactly zero in the entire domain. If we can ensure that the divergence of the coefficients is zero we successfully constrain divergence in the entire field.

Instead of simply removing divergence from the final result given by the optimizer we more closely incorporate this constraint into the optimization procedure. For the gradient based optimization techniques utilized, the optimizer is provided with a starting solution and the current gradient of the cost function with respect to the state vector for each iteration step. Assuming for the moment the use of simple gradient descent. If we provide a starting solution that is divergence free as initial state and then subtract a scaled gradient for the descent this next state is no longer necessarily divergence free. We can enforce this by requiring the gradient to be divergence free as well. If we perform an orthogonal projection of the gradient into the divergence free subspace the optimizer is never able to leave this subspace as any movement away from the initial solution is at most a linear combination of vectors from within the subspace. This not only ensures that the final result must be divergence free, but also that the optimizer is constrained in every intermediate step of the way thus eliminating these unnecessary degrees of freedom. The optimizer is simply unable to explore physically infeasible areas of the solution space. In the actual implementation we do not use simple gradient descent but the quasi newton method L-BFGS (Liu & Nocedal, 1989). The above approach is still valid since L-BFGS uses a linear combination of previous gradients for its step so it is still unable to leave the divergence free subspace at any time.

The divergence free projection is based on the Helmholtz-Hodge decomposition of a vector field into a solenoidal (divergence free) part u_{sol} and an irrotational part u_{irrot}:

$$\vec{u} = \vec{u}_{sol} + \vec{u}_{irrot} = \vec{u}_{sol} + \nabla\phi \quad (5)$$

with some yet to be determined potential field ϕ. Taking the divergence of (5) gives a Poisson equation for ϕ since $\nabla \cdot \vec{u}_{sol} = 0$:

$$\nabla \cdot \vec{u} = \Delta\phi \quad (6)$$

Once ϕ is known the divergence free part of $\vec{u}$ can be determined:

$$\vec{u}_{sol} = \vec{u} - \nabla\phi \tag{7}$$

We are solving (6) efficiently under homogeneous Dirichlet boundary conditions using a Discrete Sine Transform. This process then forms an orthogonal projection of a vector field $\vec{u}$ into the divergence free subspace.

2.2.3 Linear mode

By this approach the only needed term in the cost function is the velocity discrepancy between field and particles, however a regularization term that penalizes high wavenumber oscillations of the coefficients is still added just as in prior FlowFit versions. The cost function for the linear mode FlowFit3 thus becomes:

$$cost_{lin}(\vec{s}) = \frac{1}{2}(\| vel_{err}(\vec{s}) \|^2 + \alpha \| hfpen(\vec{s}) \|^2) \tag{8}$$

with $\vec{s}$ as the optimizer state in form of the velocity coefficients, vel_{err} as the velocity discrepancy of the particles to the field, *hfpen* as the high wavenumber penalization with a weighting term α. This penalization is calculated just as in FlowFit2 as the L2 norm of the high-pass-filtered version of the coefficient field (Gesemann et al., 2016).
This variant of FlowFit3 provides a very efficient way to perform data assimilation but does not yet use acceleration information in order to further improve assimilation quality or provide pressure reconstruction as well. This is realized in a second mode we call nonlinear mode FlowFit3.

2.2.4 Nonlinear mode

If acceleration measurements are available we can use them to further improve reconstruction quality as well as to recover pressure fields. The additional data allows for the use of the momentum equation from the incompressible Navier-Stokes equations in addition to the continuity equation used so far. Accelerations obtained from LPT measurements provide the material derivative of velocity, the left side of the momentum equation:

$$\vec{a} = \frac{D\vec{u}}{Dt} = -\nabla\overline{p} + v\Delta\vec{u} = \frac{\partial\vec{u}}{\partial t} + (\vec{u}\cdot\nabla)\vec{u} \tag{9}$$

Just as the continuity equation requires zero velocity divergence, the divergence of the temporal derivative of velocity must vanish as well:

$$\nabla \cdot \frac{\partial u}{\partial t} = \nabla \cdot (\vec{a} - \vec{u} \cdot \nabla\vec{u}) = 0 \tag{10}$$

After some transformations this leads to the Poisson equation for pressure:

$$\Delta p + \nabla \cdot (\vec{u} \cdot \nabla\vec{u}) = 0 \tag{11}$$

$$\nabla \cdot (\vec{u} \cdot \nabla\vec{u}) = \left(\frac{\partial u}{\partial x}\right)^2 + \left(\frac{\partial v}{\partial y}\right)^2 + \left(\frac{\partial w}{\partial z}\right)^2 + 2\left(\frac{\partial u}{\partial y}\frac{\partial v}{\partial x} + \frac{\partial u}{\partial z}\frac{\partial w}{\partial z} + \frac{\partial v}{\partial z}\frac{\partial w}{\partial y}\right) \tag{12}$$

The nonlinear source term can be further simplified (12) and is the origin for the naming of this mode as "nonlinear". Once the pressure field has been determined one can calculate the acceleration field as needed using (9) in order to be able to calculate an acceleration error at the particle positions. Whereas prior FlowFit versions would add an additional set of pressure coefficients to be optimized alongside the velocity the new FlowFit3 approach does not include them in the state vector anymore. Pressure is calculated from velocities by use of the pressure Poisson equation as needed which is solved efficiently using a FFT based approach. We utilize a Discrete Sine Transform (DST) which implies homogeneous Dirichlet boundary conditions. While this allows for a very efficient computation of the solution for the Poisson equation it is not necessarily the correct boundaries for a given reconstruction. To allow for arbitrary boundary conditions while still using the DST we add an inner boundary layer to the source term. Due to the support region of the B-Splines the nonlinear term can only be computed from velocity in the interior region. By surrounding this region with the additional boundary layer we retain the correct size in order to reuse the DST for the divergence free projection, now just with a different transfer function in Fourier space. By selecting appropriate values for this layer of source terms we can enforce arbitrary boundary conditions for the original problem. These explicit source term variables are simply included into the optimizer state in order to obtain suitable values for a given reconstruction problem.

With this Ansatz pressure is no longer part of the state of the optimizer (except for boundary conditions) but this approach introduces greater complexity in the implementation of the cost function and especially its gradient. Instead of just backpropagating cost function gradients to the pressure coefficients as in prior FlowFit versions they now need to be calculated further through the pressure reconstruction all the way to the velocity coefficients instead. But again, just as with the divergence constraint, the degrees of freedom for the optimizer are reduced since this way the dependent relationship between velocity and pressure is encoded explicitly. The cost function for the nonlinear mode is very similar to the linear mode (8):

$$cost_{lin}(\vec{s}) = \frac{1}{2}(\| vel_{err}(\vec{s}) \|^2 + \alpha \| hfpen(\vec{s}) \|^2 + \beta \| acc_{err}(\vec{s}) \|^2) \qquad (13)$$

now including an additional acceleration discrepancy term acc_{err} with a weighting factor between velocity and acceleration errors β. This factor can be determined from the uncertainty quantification based on the Trackfit (Gesemann et al. 2016) approach.

One could obtain the required cost function gradient with respect to the state required for the optimizer using automatic differentiation on an implementation of (12). Our implementation uses a handwritten backpropagation approach for efficiency reasons. The initial two terms also present in the cost function for the linear mode in (8) are fairly straightforward to handle since they either directly or almost directly operate on the velocity coefficients. The acceleration term is more complex so we will discuss its gradient in more detail. The cost term for the acceleration is a sum of acceleration errors over all particles:

$$\frac{1}{2}\sum_i^N \left\| a_{fitted|pos=particlepos[i]} - a_{particle[i]} \right\|^2 \qquad (14)$$

A gradient of sums is the sum of its gradients so in the following we look at the cost contribution of just a single particle within the sum with its measured acceleration $\vec{a}_p$ and the fitted acceleration $\vec{a}_f$ at its position:

$$C_a = \frac{1}{2}\left\|\vec{a}_f - \vec{a}_p\right\|^2 = \frac{1}{2}\|\overrightarrow{err}\|^2 \tag{15}$$

We can only affect this by modifying the fitted acceleration:

$$\frac{\partial C_a}{\partial \vec{a}_f} = \overrightarrow{err}\left(\frac{\partial \vec{a}_f}{\partial \vec{a}_f} - \frac{\partial \vec{a}_f}{\partial \vec{a}_p}\right) = \overrightarrow{err} \tag{16}$$

Which can be related to the velocity coefficient field $\vec{u}_k$ by chaining the Jacobians of the intermediate operations:

$$\frac{\partial C_a}{\partial \vec{u}_k} = \frac{\partial C_a}{\partial \vec{a}_f}\frac{\partial \vec{a}_f}{\partial \Delta\vec{u}}\frac{\partial \Delta\vec{u}}{\partial \vec{u}_k} \text{ with } \frac{\partial \vec{a}_f}{\partial \Delta u} = v - \frac{\partial \nabla p}{\partial \Delta\vec{u}} \text{ since } \vec{a}_f = v\Delta\vec{u} - \nabla p \tag{17}$$

The term $\frac{\partial \Delta\vec{u}}{\partial \vec{u}_k}$ is known from the B-spline construction but $\frac{\partial \nabla p}{\partial \Delta\vec{u}}$ must still be determined. Using the nonlinear term (12) as N and the Poisson solver including the mapping to the B-Spline coefficients as P we obtain:

$$\Delta p = N(\nabla\vec{u}) \text{ and } p_k = P(\Delta p) \tag{18}$$

We can then express the missing term in terms of known operations after some chain rule wrangling of the derivatives:

$$\frac{\partial \nabla p}{\partial \Delta\vec{u}} = \frac{\partial \nabla p}{\partial p_k}\frac{\partial \mathrm{P}}{\partial \Delta p}\frac{\partial \mathrm{N}}{\partial \nabla\vec{u}}\frac{\partial \nabla\vec{u}}{\partial \Delta\vec{u}} \tag{19}$$

Substituting into (17):

$$\frac{\partial C_a}{\partial \vec{u}_k} = \frac{\partial C_a}{\partial \vec{a}_f}\left(v - \frac{\partial \nabla p}{\partial p_k}\frac{\partial \mathrm{P}}{\partial \Delta p}\frac{\partial \mathrm{N}}{\partial \nabla\vec{u}}\frac{\partial \nabla\vec{u}}{\partial \Delta\vec{u}}\right)\frac{\partial \Delta\vec{u}}{\partial \vec{u}_k} \tag{20}$$

followed by simplification of some $\vec{u}, \vec{u}_k$ terms and substituting (16) one finally obtains:

$$\frac{\partial C_a}{\partial \vec{u}_k} = \overrightarrow{err}\frac{\partial \Delta\vec{u}}{\partial \vec{u}_k}v - \overrightarrow{err}\frac{\partial \nabla p}{\partial p_k}\frac{\partial \mathrm{P}}{\partial \Delta p}\frac{\partial \mathrm{N}}{\partial \nabla\vec{u}}\frac{\partial \nabla\vec{u}}{\partial \vec{u}_k} \tag{21}$$

the desired gradient of the acceleration cost function with respect to the optimizer state in form of the velocity coefficients. One essentially multiplies this from left to right as vector Jacobi products (*vJp*) starting from the calculated acceleration error value at the particle location $\overrightarrow{err}$. The Jacobi matrices in (21) are not supposed to be actually created as one can implement the result of the *vJp* directly. These adjoints generally can be obtained for a similar computational cost as the respective operations in the forward pass. This is especially the case for the Poisson solver step P as it is self-adjoint. At that stage of the backpropagation one would also extract the gradient for the source term used for the pressure boundary. As the value of the source term is jointly optimized together with the

velocity coefficients one needs to scale its gradient to a similar norm as the gradient for the velocity coefficients.

3 Evaluation

To compare the new FlowFit3 variants to the prior versions we use synthetic data based on a sub-volume of the isotropic turbulence data set from the Johns Hopkins Turbulence Database (Yeung et al. 2012) just as in the original FlowFit2 publication (Gesemann et al. 2016). Synthetic particle data is generated simply by sampling the database at random positions in the domain. Four different particle densities are investigated resulting in a mean inter-particle distance of approx. 7.5 to 3.75 Kolmogorov length scales. We compare the performance of FlowFit3 with results obtained using the FlowFit2 approach on the same data. Figure 2 shows a comparison of reconstruction quality in a slice of the vorticity field for a particle sampling at 6 Kolmogorov length scales. The FlowFit2 div1 version, using only velocity information, yields the lowest quality of reconstruction.

Interestingly, the linear version of FlowFit3 shows visibly better results, despite depending on the same restricted data. The div2 variant of FlowFit2, additionally utilizing acceleration data, markedly improves on its div1 counterpart, producing results quite alike to FlowFit3 linear, albeit with a slightly better rendition of the gradient. The FlowFit3 nonlinear mode yields a further increase of perceived sharpness.

This can also be seen in a visualization of iso-surfaces of the Q-criterion of the same reconstructions, but at a reduced particle density to a mean spacing of approx. 7.5 Kolmogorov length scales shown in Figure 3. Again, the nonlinear mode FlowFit3 provides a slight improvement over FlowFit2 div2 whereas a significant gain can be observed for the linear mode versus the div1 result. This highlights the benefit of including acceleration data using the momentum equation. Both FlowFit variants using accelerations are much less affected by the decrease of particle density than the variants using only velocity. The FlowFit2 div1 result has degraded significantly. Linear mode FlowFit3 now shows less detail than the nonlinear variant but still presents a relatively smooth solution without the noise visible for div1 FlowFit2.

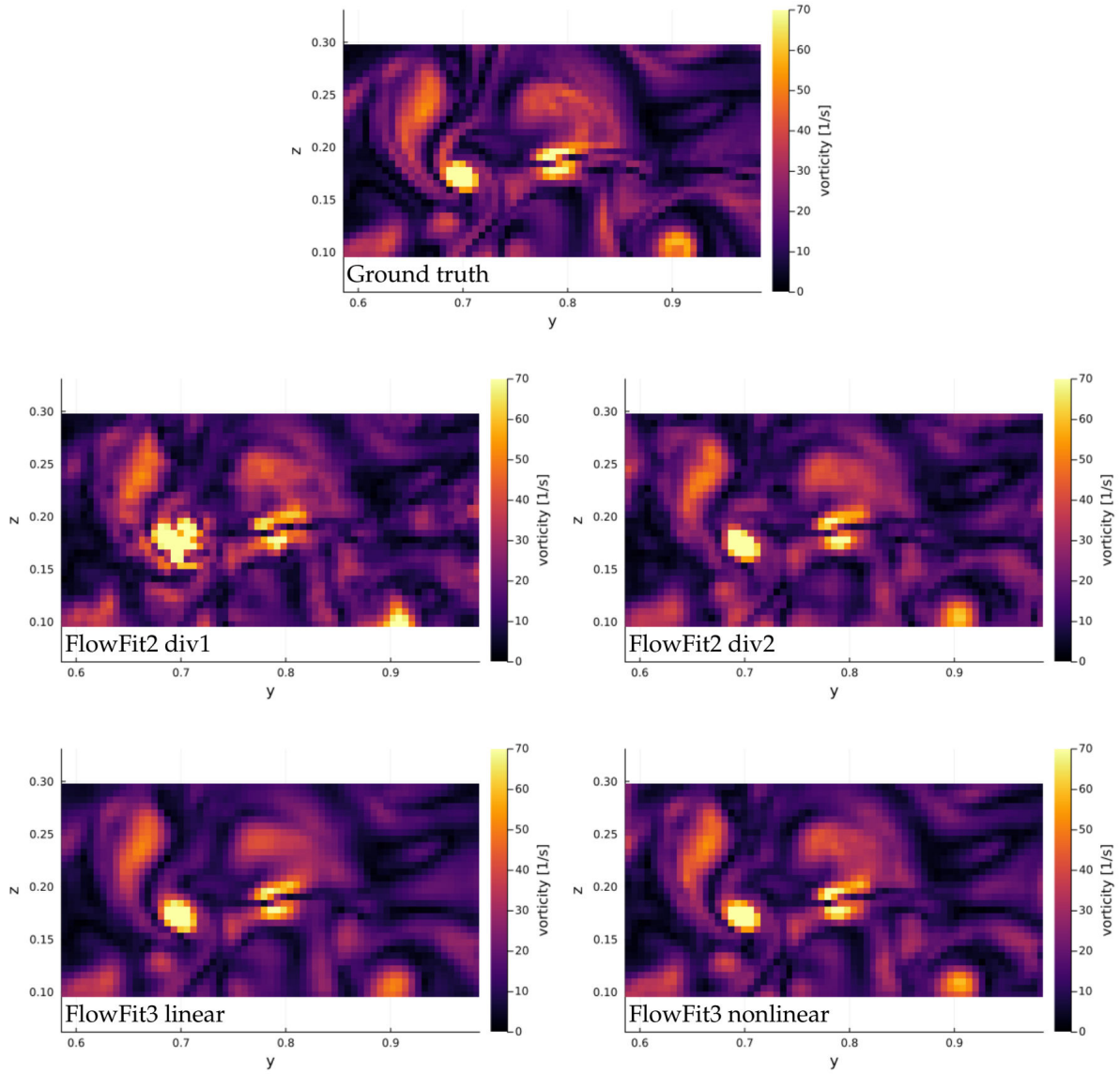

Figure 2: Slices of vorticity field reconstructed using the different methods for a particle density with a mean spacing of approx. 6 Kolmogorov length scales

A quantitative comparison of rms-errors of the Q-value compared to the ground truth is presented in Figure 4 for a range of particle densities. The results match the visual interpretations of the prior figures with FlowFit3 nonlinear as an improvement over FlowFit2 div1. As the particle distance increases the difference between the variants with and without use of the momentum equation increases. Remarkable is the comparatively low error of the FlowFit3 linear mode which almost approaches the performance of the prior FlowFit2 div2 version, but at much lower computational costs.

A brief evaluation of the reconstructed pressures shows the handling of arbitrary boundary conditions in FlowFit3 non-linear mode is successful. Figure 5 shows the error of reconstructed pressure in a slice through the volume. The FlowFit2 div2 result shows a slight gradient in the error field which is not present in the FlowFit3 non-linear case. The architectural changes to the FlowFit internals in the handling of the divergence constraint appear to be highly successful in guiding the optimizer towards a physically correct solution. Such performance makes the linear mode very attractive for the processing of a large number of snapshots as it is very efficient. On a reasonably modern CPU, a typical measurement domain can usually be reconstructed in less than 10 seconds, while the nonlinear mode requires around one order of

magnitude more processing resources. However, compared to other data assimilation methods, even this mode is highly competitive in terms of computational cost, as reported in Zhou et al. 2024. Some aspects of the nonlinear mode are still under development so we still expect some improvements to the above results.

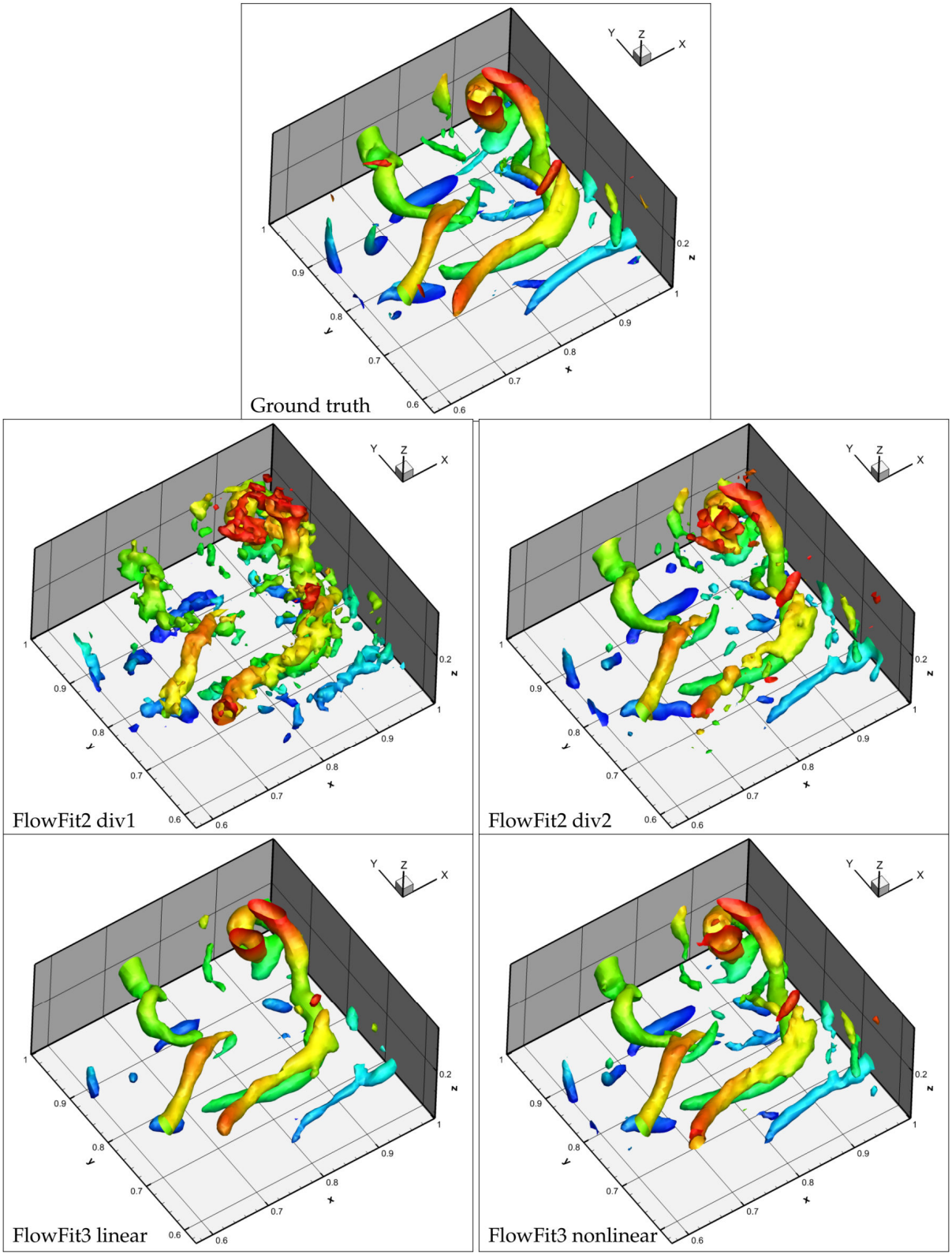

Figure 3: Iso-surfaces of Q-criterion at 400 1/s2 reconstructed using the different methods for a particle density with a mean spacing of approx. 7.5 Kolmogorov length scales

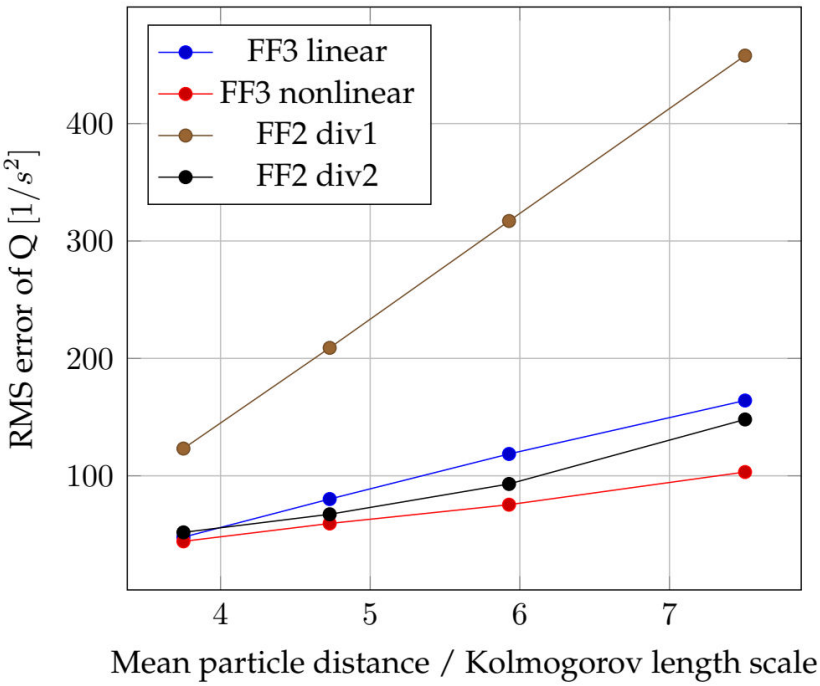

Figure 4: RMS error of the reconstructed Q field for the different methods at various particle densities

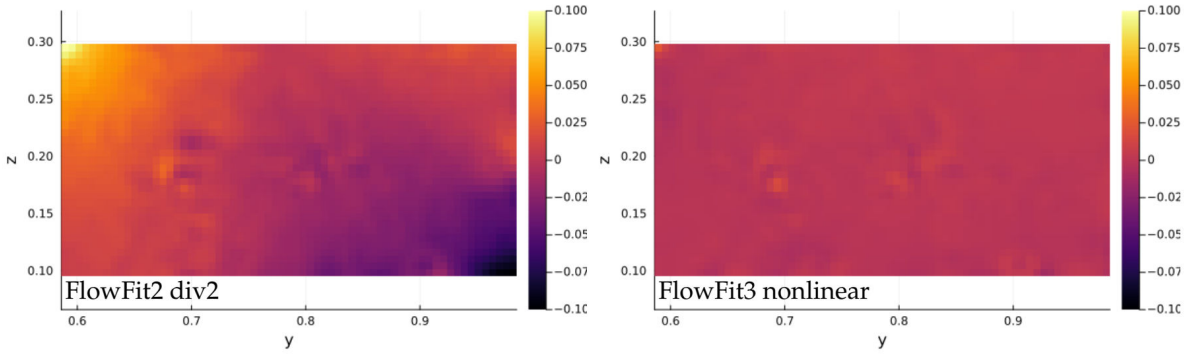

Figure 5: Pressure reconstruction error for the two methods for a particle density with a mean spacing of approx. 6 Kolmogorov length scales

4 Conclusion and future work for FlowFit3

Based on the initial testing presented above the new FlowFit3 approach is a successful development that outperforms its predecessor in data quality and reconstruction time. The linear mode provides very fast reconstruction times which will be of interest for large data sets. The nonlinear mode results in even higher fidelity reconstructions and also allows for pressure reconstructions. For a more detailed evaluation of the FlowFit3 variants see Zhou et al. (2024).

For the current implementation of FlowFit3 only a limited number of parameters needs to be selected. A key value that needs to be adjusted is the penalization of higher wave numbers α. This parameter directly controls the smoothness of the solution and as such can be easily adjusted based on visual examination. A current topic for further development is to better determine this regularization based on physical properties. Different regions of a flow field likely require different strengths of this regularization which could be determined from flow structure sizes obtained from two-point correlations. Currently the high-pass filter used for the

penalty operates directly on the coefficient field. In principle this would still allow for spatially varying regularization since the coefficients directly correspond to regions in physical space. However, it would be beneficial to instead define the penalization in world space in order to more precisely allow for spatially varying anisotropic curvature penalization.

Currently FlowFit3 conducts an independent reconstruction of individual time steps in a sequential measurement. This can be an advantage for parallel processing as no time resolved data is required but leaves some room for further improvement. The use of virtual particles to enhance temporal consistency has already shown some benefit (Ehlers et al. 2020) but future work will also consider more explicitly linking FlowFit3 reconstructions across multiple timesteps for a joint optimization or in conjunction with PINNs.

5 Estimation of time-resolved 3D pressure fields in an impinging jet flow from dense 3D Lagrangian particle tracking (LPT)

5.1 Introduction

The measurement of the pressure field in aerodynamic and turbulent flows is of high interest, for example, for the estimation of unsteady fluid dynamic loads and forces on structures to study aero-elastic problems, for the determination of sources of aero-acoustic noise, and for the computation of the pressure-diffusion term in the transport equation of turbulent kinetic energy. Pressure transducers and microphones can be used to obtain a local point-wise measurement of pressure. They are often mounted in walls, and also free-field pressure probes exist. However, unlike the intrusive measurement with sensors, the pressure field is also indirectly accessible through an optical nonintrusive flow measurement of fields of the material acceleration. The pressure gradient and the material acceleration are the dominant terms in the momentum equation (1) and therefore directly linked by this equation. van Oudheusden (2013) reviews the development of pressure reconstruction from flow measurements that dates back to the year 1935 and made significant progress in the last two decades, mainly based on velocity data gained from particle image velocimetry (PIV).

Recent examples of studies dealing with pressure reconstruction from flow measurements include a comparison of stereoscopic and tomographic (tomo) PIV in the wake of a square cylinder de Kat and van Oudheusden 2012, tomo PIV measurements in a turbulent boundary layer (Ghaemi et al. 2012, Pröbsting et al. 2013, Schneiders et al. 2016), time-resolved tomo-PIV around an airfoil (Jeon et al. 2015), a scanning tomo PIV experiment around a flapping wing (Tronchin et al. 2015), a tomo-PIV measurement with subsequent particle tracking in the wake of a wall-mounted cylinder (Schneiders et al. 2016, cf. Li et al. 2008, Schneiders et al. 2016). Most of the studies validate their results against other pressure measurements or against theoretical predictions. Except for the last two, the listed studies are based on time-resolved PIV data and consequently obtain the material acceleration from the Eulerian velocity field by computing the low-pass filtered material derivative indirectly. A comparison of a broad scope of techniques for pressure reconstruction (van Gent et al. 2017) shows, however, that the accuracy of the pressure field determination can be considerably improved with dense Lagrangian particle tracking (LPT) where the material acceleration is directly obtained from individual particle trajectories. Nowadays, with the Shake-The-Box (STB) Lagrangian particle tracking technique (Schanz et al. 2013, Schanz et al. 2016a, Schröder and Schanz 2023) time-resolved series of particle images with densities of ~0.1 ppp and above can be processed

accurately which allow to simultaneously track up to 300,000 particles for typical 4 Mpx high-speed cameras (Huhn et al. 2017, Bosbach et al. 2021). Furthermore, a new four-pulse STB technique is available, which allows the required determination of velocity and acceleration fields by Lagrangian particle tracking as well in high-speed flows (Novara et al. 2019). In a review article on the development of load estimation techniques Rival and van Oudheusden 2017 explicitly propose that the STB technique will become the new standard for instantaneous pressure reconstruction and state its importance for future measurements of unsteady flows.

In our experimental investigation time-resolved volumetric pressure fields have been reconstructed in a perpendicular impinging jet flow with exit velocities at U =1, 4 and 16 m/s and a nozzle-plate spacing of H/D = 5 from Lagrangian particle tracking with high seeding concentration. The Shake-The-Box method has been employed for dense particle tracking and subsequently the FlowFit2 data assimilation technique has been applied to the particle track data in order to gain 3D velocity and pressure fields. Helium-filled soap bubbles (HFSB) are used as tracer particles (Bosbach et al. 2009) which are illuminated by high-power pulsed LED arrays at 1.25 kHz acquisition rate. A large measurement volume of 54 liters has been covered enabling particle tracking of up to ~190,000 particles simultaneously. The reconstructed time-resolved 3D pressure fields have been validated against local flush mounted microphone recordings at the wall with high correlation coefficients up to R = 0.88. In a reduced measurement volume (13 liters) it was demonstrated that dense Lagrangian particle tracking is feasible up to the maximal possible jet velocity of U = 16 m/s at the current set-up. This fact indicates the possibility to apply large-volume flow measurements by STB using HFSB as well in low-speed wind tunnels, in which the interference-free introduction of the HFSB tracers in a sufficient number and density is one major challenge. Further details of the present experimental investigation can be found in (Huhn et al. 2018).

The experimental set-up, acquisition strategy of particle images, STB evaluation method and post-processing steps using FlowFit2 for gaining continuous 3D velocity and pressure field reconstructions are described in section 5.2, while the gained time-resolved volumetric pressure and flow field results are presented in section 5.3 together with comparisons of sampled 3D pressure signals at the wall with time-series of pressure fluctuations measured by three flush mounted microphones.

5.2 Method

In the present study, we combine three techniques in the field of particle-based measurement methods, Shake-The-Box Lagrangian particle tracking (LPT), helium-filled soap bubbles (HFSB) and use of high-power LEDs for pulsed volumetric illumination of the bubbles in order to measure the flow of an impinging jet. The impinging jet was chosen as a generic flow with substantial pressure gradients and fluctuations that has many practical applications. An air jet generated by an 8-bladed fan with stators (PHYWE - 02742-93) and a nozzle exit diameter of 0.11 m impinges on a flat acrylic glass plate at an angle of $\theta = 90^{\circ}$. The flow is seeded with HFSBs with a diameter of 300 -*500* μm depending on the air pressure supplied to the generator (LaVision HFSB generator, 10 nozzles). For a single measurement run, the flow chamber was seeded in advance for a time > 5 min and the seeding generator was left running during the measurement. The HFSBs are illuminated by three over-pulsed high-power LED arrays, including two arrays of 42 LEDs each (HARDsoft Microprocessor Systems) operated at 90 A

(voltage 44 V). The illuminated cross-sectional area has a size of ~200 mm in depth and ~450 mm in radial direction along the glass plate. All LED arrays are equipped with collimating lenses on top of each single LED and are operated at 10% duty cycle. A rectangular mirror on the bottom plate is used to increase the illumination by back reflection.

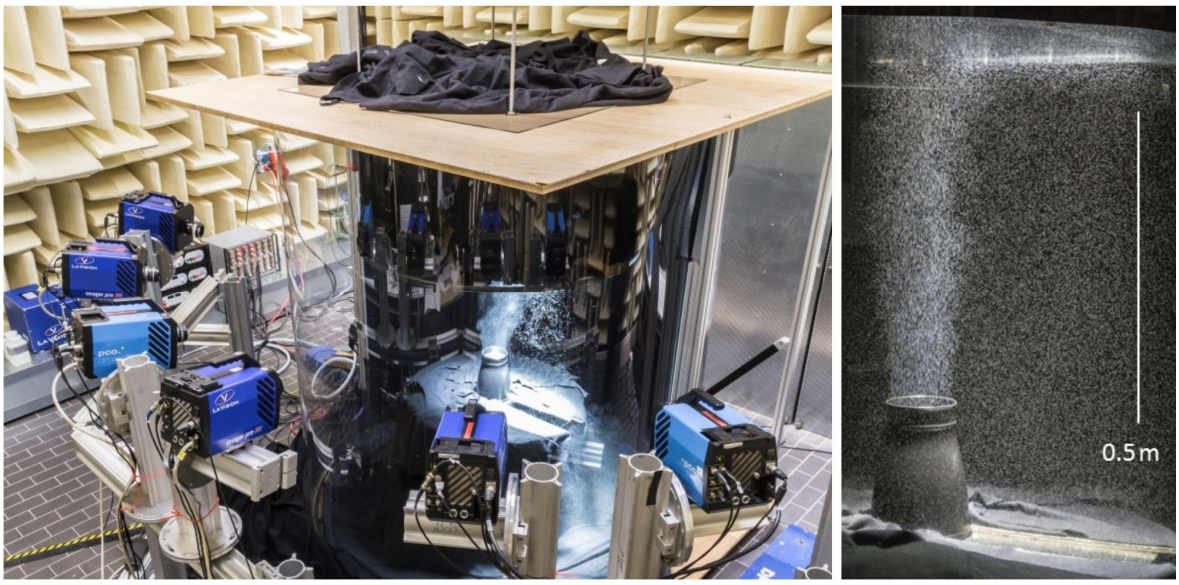

Figure 6: Experimental setup. (a) Camera setup and flow chamber. (b) Jet nozzle and impinging jet seeded with HFSB tracers. At the top, the locations of the three microphones in the impingement plate appear as bright dots.

The measurement volume, extending from the wall to the fan nozzle exit (530 mm in streamwise direction) is imaged by six high-speed cameras (PCO Dimax S4 and LaVision Imager pro HS 4M). The cameras are positioned in an in-line configuration and oriented in a way that those lines-of-sight imaging the wall surface are tangential to the flat plate. For the calibration of the cameras, a large 2D calibration target (77 × 95 cm^2, black dots, diameter 10 mm, spacing 45 mm) on a translation stage is aligned with the centerline of the jet and is translated -100 mm and +100 mm in z-direction. Volume self-calibration (VSC) (Wieneke 2008) is used to refine the camera calibration. The experimental setup is shown in Figure 6.

The STB evaluation technique has been adapted to the series of particle images from all 6 camera projections, which requires the calibration of the particles optical transfer function (OTF) for each camera and sub-volume (Schanz et al. 2013) and a proper parametrization of the iterative 3D particle reconstruction scheme (IPR) (Wieneke 2013), Jahn et al. 2021) for the initialization phase of STB and the 3D particle position correction ("shaking") after each prediction step. Particle tracks with discrete positions are then fit with a continuous function consisting of cubic B-splines (TrackFit, Gesemann et al. 2016). The coefficient for the smoothing term in the cost function is based on the cross-over frequency of the particle position frequency spectrum and is chosen such that particle tracks are low-pass filtered with a cut-off frequency of $0.3f_{Ny}$ with the Nyquist frequency f_{Ny} . Velocity and acceleration are obtained as the temporal derivatives of the continuous B-spline function. With a model for the position frequency spectrum of the found tracks assuming the jolt of the used measurement signal to be white noise, the uncertainties of position, velocity and acceleration of the fitted trajectories

(TrackFit) can be estimated as ε_x = 16 µm (~ 0.05 pixels), ε_v = 0.01 m/s and ε_a = 14 m/s² for the U = 4 m/s flow case. For the low velocity case at U = 1 m/s the respective uncertainties are ε_x = 8 µm, ε_v = 0.002 m/s and ε_a = 0.8 m/s², and for the fast case at U = 16 m/s they are ε_x = 28 µm, ε_v = 0.07 m/s and ε_a = 375 m/s². On one side, the reduction of position accuracy for increasing velocities are caused by the reduced amount of light available per snapshot at respective higher illumination and imaging frequencies. On top of that an increase in position, velocity and acceleration uncertainties is caused by the relative reduction of the sampling frequencies with respect to the smallest temporal scales within the turbulent flows which typically decrease with increasing Reynolds number. This leads to the conclusion that depending on the (local) spectrum of the flow a Lagrangian particle tracking experiment needs increase the imaging frequency more than linear with the velocity and/or Reynolds number (as typical in PIV for keeping a constant pixel shift between two time-steps) in order to reconstruct the corresponding 3D pressure fields adequately. The respective scaling properties have to consider the actual Kolmogorov lengths and time scales.

In general, STB Lagrangian particle tracking with high seeding densities is well suited for the measurement of mean fields in the flow. Bin averaging of velocity and acceleration, that are accurately measured based on single trajectories with subpixel (~0.1 px) position accuracy, yields mean fields (Schröder et al. 2015). Due to the large number of particles, a high spatial resolution (typically with subpixel bin sizes) of the mean and related RMS- fields and a small uncertainty (many particles per bin) can be reached with reasonable experimental effort. Due to the high position accuracy, the mean acceleration field can be obtained down to walls, such that mean wall pressure fields on aerodynamic models are obtained by a simple integration of the mean acceleration field.

Based on our measured time-resolved velocity and acceleration data along the densely distributed tracks instantaneous 3D pressure fields are reconstructed in a next step with the interpolation and data assimilation scheme FlowFit2 (Gesemann et al. 2016). In the FlowFit2 approach both measured fields, velocity u and acceleration a, and the full momentum equation

$$\vec{a} = \frac{D\vec{u}}{Dt} = -\nabla\overline{p} + v\Delta\vec{u} = \frac{\partial\vec{u}}{\partial t} + (\vec{u}\cdot\nabla)\vec{u} \tag{22}$$

coupling both measured quantities are considered for the pressure reconstruction.

The two fields $\vec{u}$ and $\overline{p}$ are used as fit variables. Acceleration is expressed in terms of $\vec{\boldsymbol{u}}$ and $\overline{p}$ by Eq. (22). The velocity field is regularized by $\nabla\cdot\vec{u} = 0$. Combining the further condition $\nabla\cdot\frac{\partial\vec{u}}{\partial t} = 0$, with the material derivative and the momentum equation leads to the condition $\Delta\overline{p} + \nabla\cdot(\vec{u}\cdot\nabla)\vec{u} = 0$ for the two fit variables. This last condition is quadratic in $\vec{u}$ and leads to a non-linear optimization problem which is solved with a Limited-memory Broyden-Fletcher-Goldfarb-Shanno (L-BFGS) solver (see Gesemann et al. 2016). At the wall we impose symmetric boundary conditions, i.e., the measured flow quantities $\vec{u}$ and $\vec{a}$ are mirrored at the wall, i.e., about the *x–z* plane. These boundary conditions correspond to setting the normal vector components of velocity and acceleration to zero at the wall, $u_{y|w}$ = 0 and $a_{y|w}$ = 0, where the *w*-subscript denotes the evaluation at the wall. For the simpler momentum Eq. (22) this

translates to the condition $\frac{\partial p}{\partial y}|_w = 0$. This is in line with the observation that in a turbulent boundary layer the pressure at a small distance to the wall is a good estimate for the wall pressure itself (Pröbsting et al. 2013). Applying the above estimated uncertainty values found for particle velocity and acceleration to the calculation of the error of the pressure reconstruction for a corresponding wavenumber window between two times the mean particle distance, λ_2 = 12 mm and a typical domain size, λ_1 = 200 mm, i.e., [k_1, k_2] = [31, 524] rad/m the uncertainty of the pressure field remains in the order of $\sigma_N \sim 0.1$ Pa (details in (Huhn et al. 2018). This uncertainty seems rather small and would correspond to a dynamic pressure range of ~ 60:1. However, it is a rough estimate and additional error sources may exist. On one hand, aliasing due to under-sampling of small flow structures possibly leads to an additional error that is excluded in the above value. On the other hand, with STB the 3D pressure measurement uncertainty is scalable: At lower flow velocities much smaller pressure fluctuations are measurable which is caused by the lower uncertainties of velocity and acceleration determined at U = 1 m/s.

The interpolated pressure and velocity fields are represented as a dense grid of cubic B-splines with a step width of Δx = 3 mm, half the mean particle distance of 6 mm, corresponding to a particle density of 0.125 particles per B-spline cell [ppc]. The B-spline coefficients are found by a fit to the scattered data. The cost functions include terms for spatial smoothing and for a regularization of the solution with additional physical constraints from the Navier-Stokes-equation. The wall allows for the installation of microphones for a validation of the pressure reconstruction. Three condenser microphones (G.R.A.S. 40BF 1/4", diameter of diaphragm 5.9 mm) are flush mounted in the impinging plate at distances of 1*D*, 2*D* and 3*D* from the jet center. The frequency response is flat (±2 dB) in the range from 4 Hz to 100 kHz. Microphone data is recorded with a 16-bit VIPER- 48 (GBM) multi-channel acquisition system at a frequency of 250 kHz, high-pass filtered with a 1.5 Hz cut-off frequency. Microphone recordings are synchronized with the flow measurement by recording the trigger (enable) signal of the LED illumination on an additional channel. Noise from the fan and its motor is the main source of uncertainties of the microphone pressure signal. However, in the relevant frequency range of 5–150 Hz, the signal to noise ratio has been measured to be in the order of 10^4, i.e., the amplitude error of the microphone pressure signal is ~ 1% and therefore negligible w.r.t. the accuracy discussed here.

The study has two objectives, first, we show the applicability of LPT with LED illuminated HFBSs in a large volume for higher flow velocities than in previous experiments (Huhn et al. 2017), and second, we validate the reconstructed pressure field. We achieve a measurement volume of 54 liters for a jet velocity of U = 1 and 4 m/s and a rectangular volume of 13 liters at U = 16 m/s with a reduced field-of-view due to frame rate limitations. To the best knowledge of the authors, the reconstructed volumetric pressure field with a volume of 30 liters is the largest reported so far (cf. Rival & van Oudheusden 2017, Schneiders et al. 2016, van Oudheusden 2013).

5.3 Assessment of pressure reconstruction via FlowFit2

Synthetic experiments using the FlowFit algorithm have been performed based on a subvolume of the DNS data of the "Forced Isotropic Turbulence" case at Re_λ = 418 from the

Johns Hopkins Turbulence Data Base (FIT@JHTB, Li et al. (2008)) in order to assess the accuracy of the reconstructed velocity and pressure fields. A set of randomly selected DNS data points with different numbers and densities (resp. mean data point distances) are used in order to mimic a Lagrangian particle tracking experiment encountering the usual problem of undersampling the flow and pressure structures in turbulence. FlowFit2 reconstructs the full flow field based on the sparse scattered data points providing velocity and acceleration as input to the non-linear data assimilation problem. The accuracy of the reconstructed flow field is depending on the number and density of scattered input data points which can be quantitatively assessed by comparing the gained results to the provided ground truth from DNS. The subvolume size consists of 64 x 64 x 32 (= 131,072) grid points with a grid point spacing of dns_h = 2pi/1024 = 0.006136, while the Kolmogorov length scale η = 0.00280 corresponds to 0.4563·dns_h. All values are non-dimensional based on the DNS grid in time and space. Figure 7 displays the subset of randomly selected data points in the sub-volume of 3,157 points (top-left), 6,569 points (top-right), 13,104 (points) (bottom-left) together with iso-surfaces of $\frac{1}{2}\Delta\overline{p}$ assimilated and interpolated by the FlowFit2 algorithm based on the respective subset of points. Ground truth from DNS for comparison is placed bottom-right. The number of points corresponds to ~1/41.5 (top-left), ~1/20 (top-right) and ~1/10 (bottom-left) of the original DNS resolution, but the main features of the pressure field can already be reconstructed by FlowFit2 using the lower number of points.

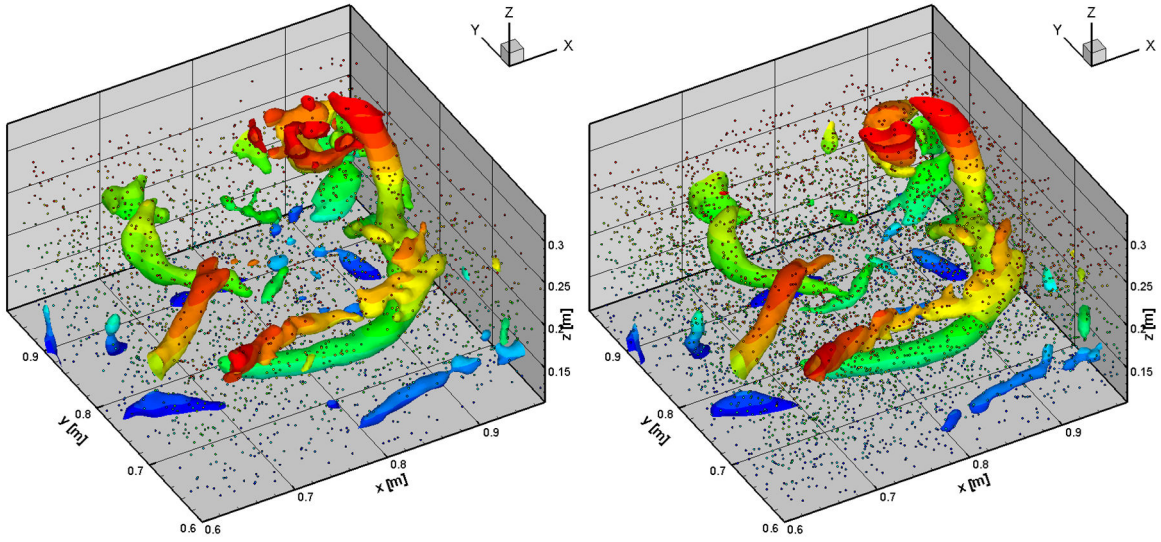

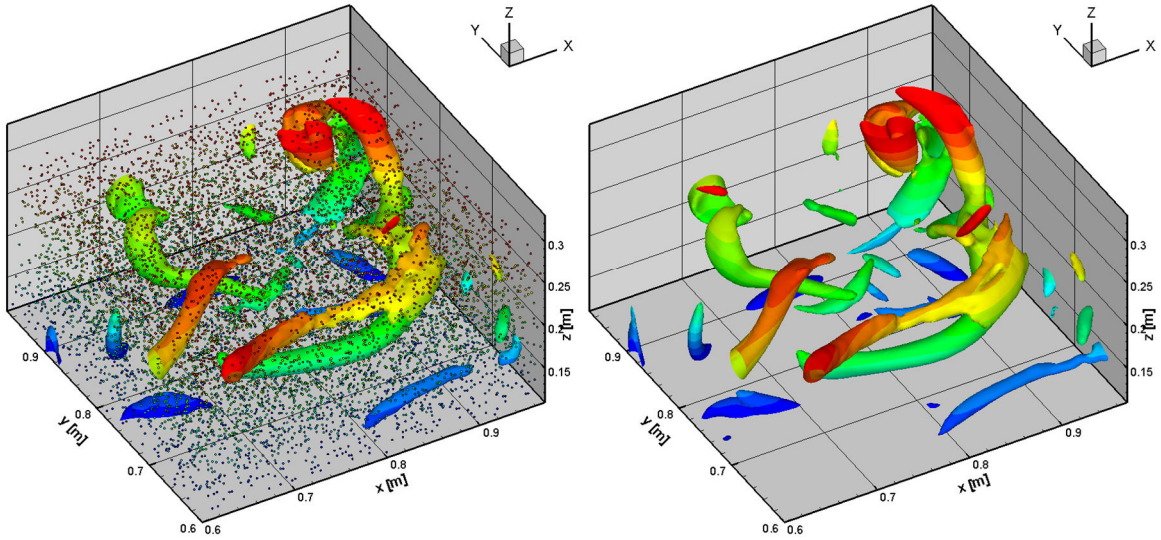

Figure 7: Iso-surfaces of $\frac{1}{2}\Delta\overline{\boldsymbol{p}}$ for reconstructed p and random sample positions of data points with color-coded z coordinate. Due to incompressibility and constant density $\frac{1}{2}\Delta\overline{\boldsymbol{p}}$ is equivalent to the Q criterion. The iso-contour level is 500 (non-dimensional by DNS grid)

~4.7 η for the higher density case. The $\sqrt[3]{n}$ –law allows one to keep the *ppp*-level of a STB experiment in a reasonable range (e.g. < 0.1 ppp) allowing for high accuracies of the velocity and acceleration measurements along the tracks. Below a certain *ppp* threshold this strategy can provide a bigger gain for the quality and resolution of the FlowFit2 interpolation than just enhancing the *ppp* to higher values and towards more difficult tracking conditions, because a higher *ppp* in the images provides just a small step in reducing the mean particle distance in 3D and will reduce the measurement accuracies.

The percentage error of the pressure and pressure gradient reconstruction by FlowFit2 with respect to the local peak values for four different numbers of random data point cases from the DNS (with an additional case at an even higher density with 26,189 data points) is shown in Figure 8. The gain in accuracies for lower particle mean distances is still significant, but is reduced. A good result with 2 % RMS with respect to local peak values can be reached already at a fraction of ~1/20 data points compared to the full DNS resolution.

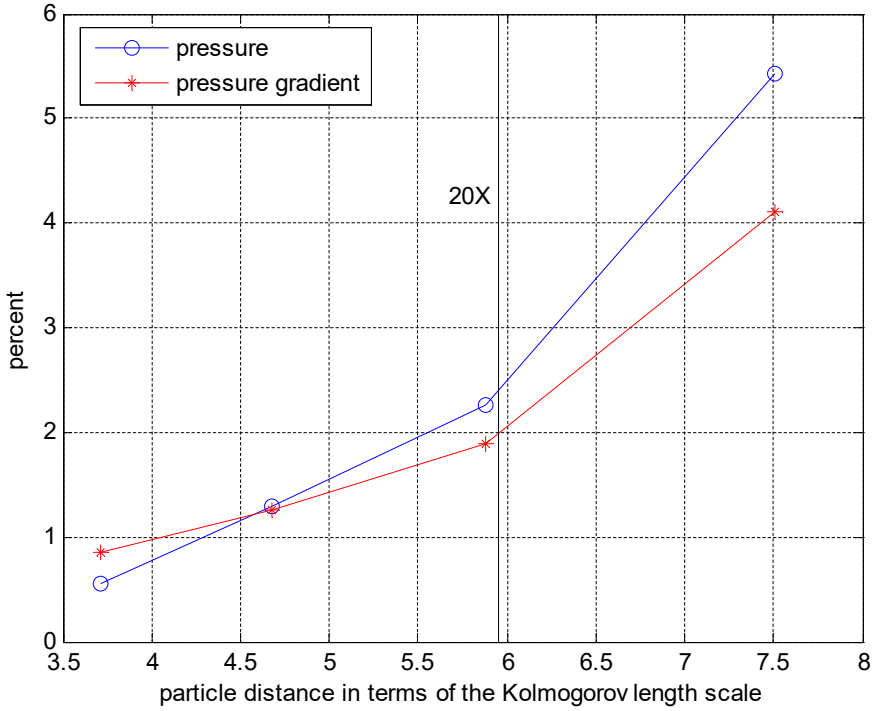

Figure 8: RMS error of reconstructed pressure and pressure gradient relative to peak spatial pressure fluctuation and peak pressure gradient, respectively. The black vertical line represents the particle distance at which the DNS grid is under sampled by a factor of 20

5.4 Results

The velocity fields of the impinging jet are presented for the slowest and fastest measured jet velocity, U = 1 m/s and U = 16 m/s. The slow case is recorded at a frame rate of 1.25 kHz with an LED pulse width of 100 µs. For the fast case, both parameters are adjusted to a frame rate of 3.9 kHz with an LED pulse width of 27 µs, in order to avoid streaking of the particle images and to reliably track also the fastest and most accelerated particles. To reach the high recording frequency, the camera resolution has to be reduced to 576 x 1728 pixels. Approximately 190,000 particles can be tracked simultaneously for the slow case in a volume of 54 liters, and 40,000 for the fast case in a volume of 13 liters. An example of the reconstructed particle tracks is shown in Figure 9.

An example of a reconstructed 3D pressure field together with the Q-value for visualization of vortical motions is presented in Figure 10. For this case at U = 1 m/s, extended spatial and temporal coherent vortical structures can be resolved in the shear layer and in the wall jet region. The rectangular box in Figure 10 marks the region of negligible flow which is used as a reference for the absolute pressure and thus as a value for the pressure off-set correction.

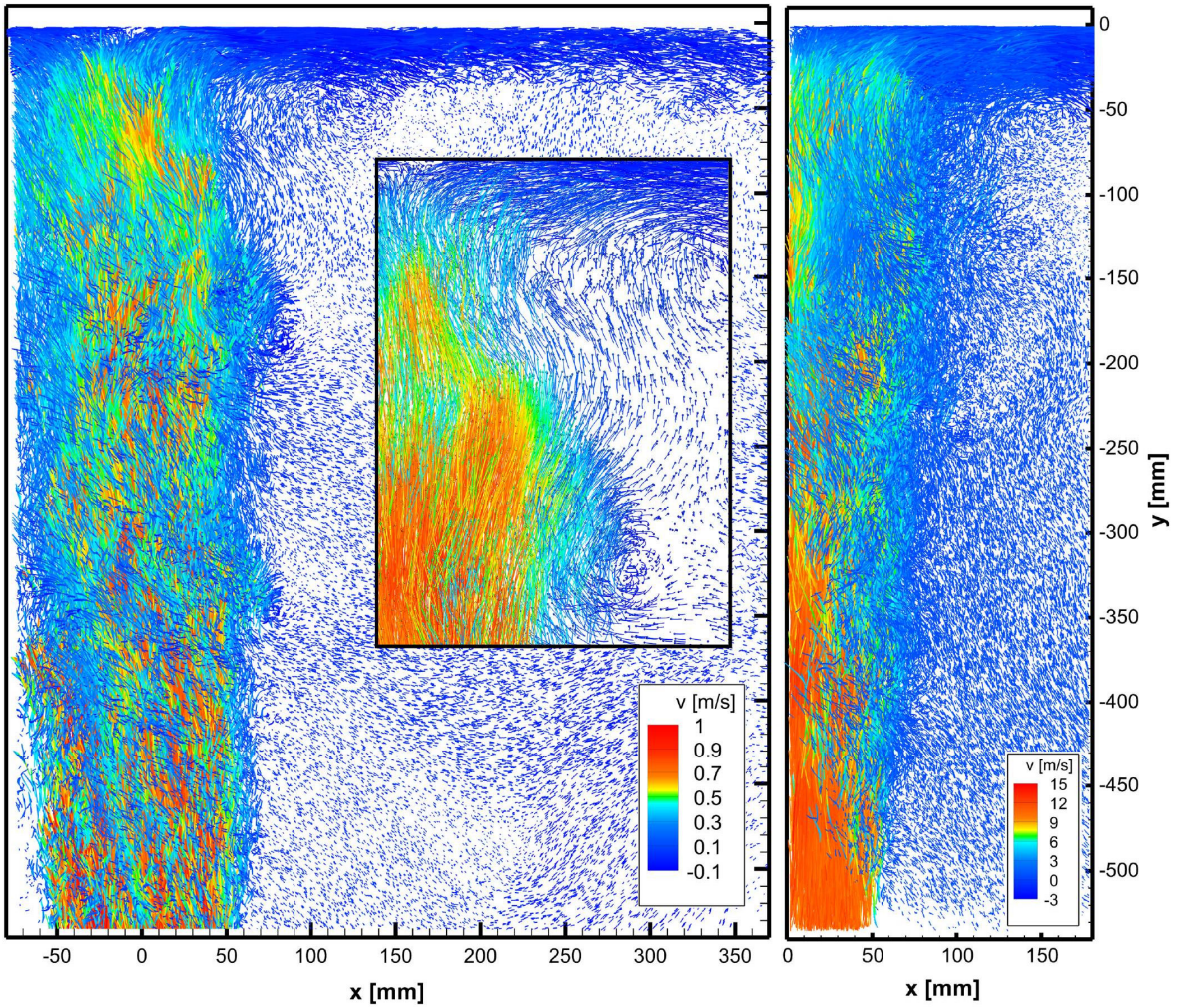

Figure 9: Lagrangian particle tracks reconstructed by Shake-The-Box displayed using nine successive time-steps, color-coded by y-velocity for two jet velocities (Left: U = 1 m/s , Right: U = 16 m/s)

In a first step the mean pressure over the box is set to be zero at each time step by subtracting the spatial mean value over the box from the entire pressure field. For the reconstruction of the pressure field, we focus on the experimental results with a jet velocity of $U = 4$ m/s recorded at 1 kHz. For this velocity, we can expect more pronounced pressure fluctuations than for the slower velocity of $U = 1$ m/s, while the appearing flow structures can be better resolved spatially and temporally with the installed measurement equipment than in the high flow velocity case at $U = 16$ m/s.

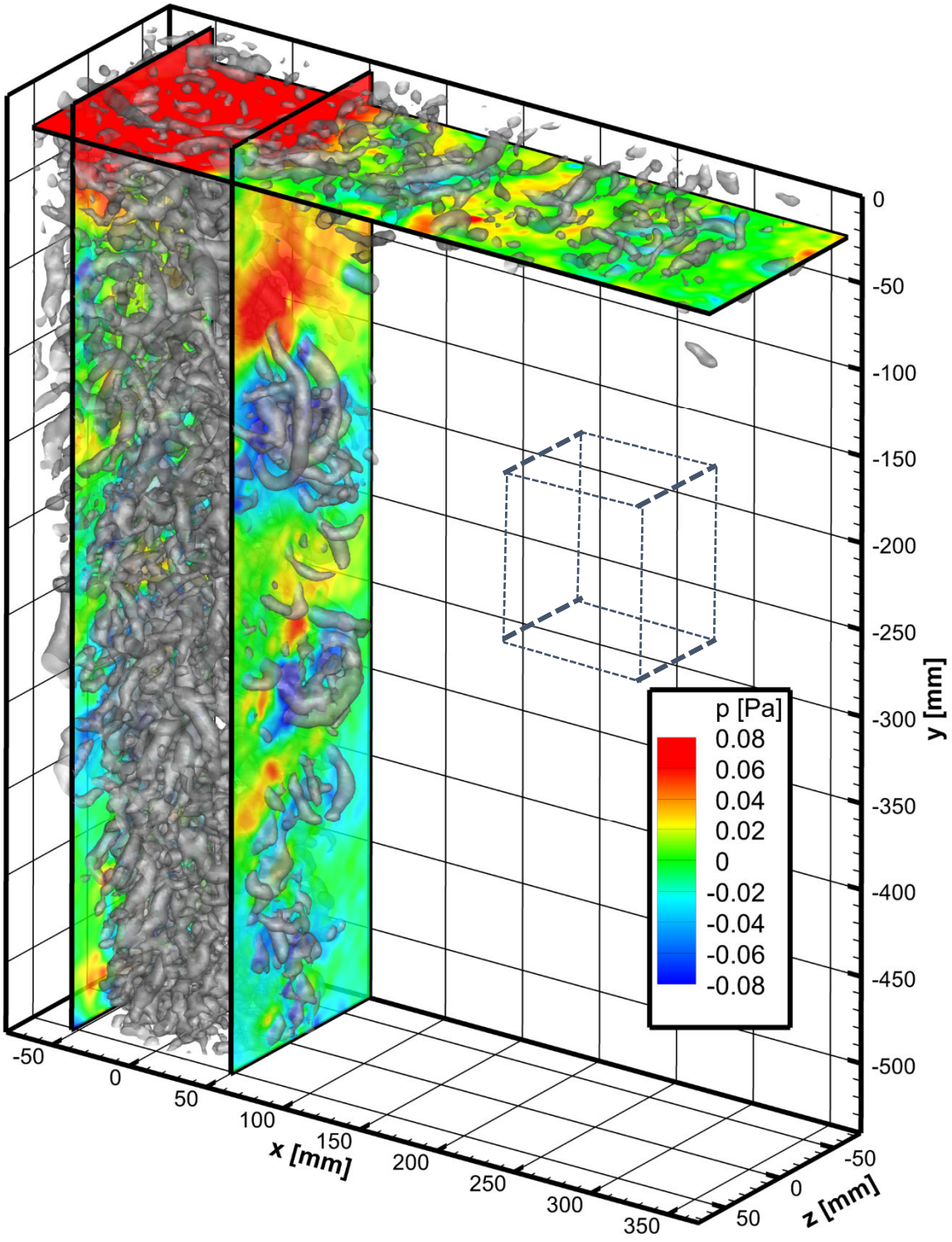

Figure 10: 3D pressure field reconstruction from STB and FlowFit2. Snapshot from a time-resolved series of impinging jet flow at U = 1 m/s with iso-contour surfaces of Q-value for visualization of vortical motions. Marked rectangular box used for pressure off-set correction.

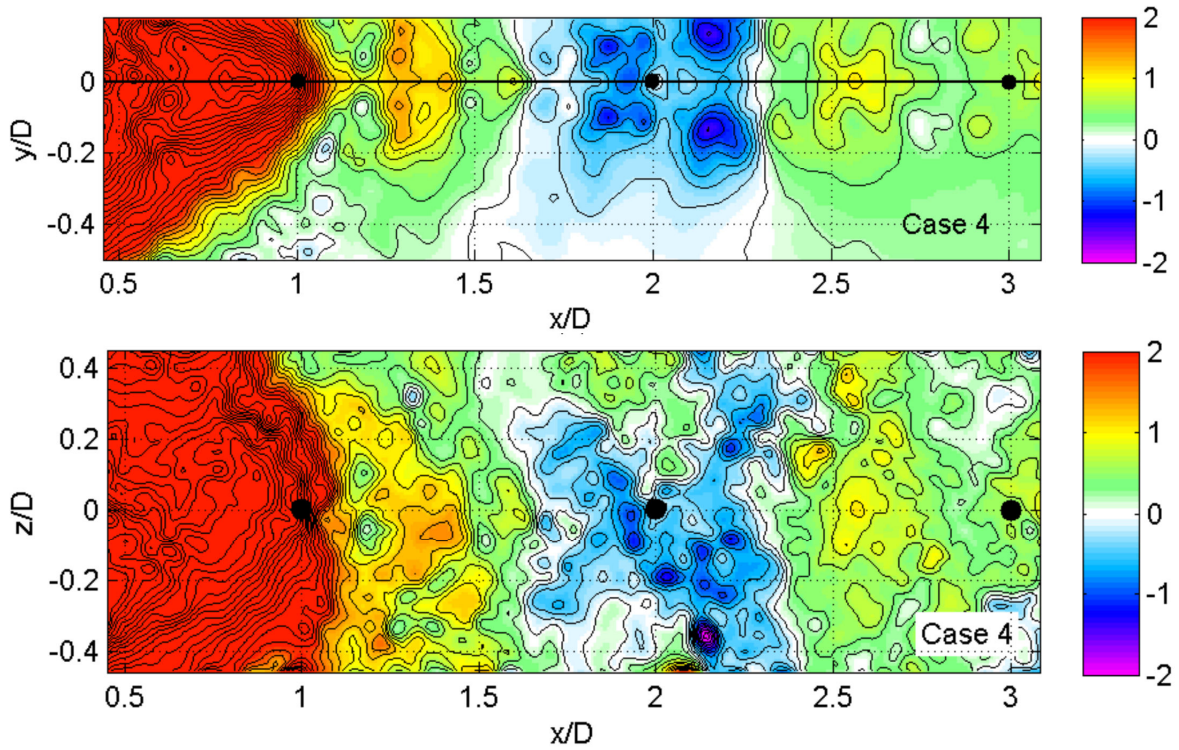

Figure 11: Lateral central slice (x-y-plane) (top) and at the wall (x-z-plane) (bottom) of the reconstructed pressure field P (x) [Pa] at U = 4 m/s using full non-linear FlowFit2 data assimilation and symmetric ("mirrored") boundary conditions at the wall. The wall is drawn as a black line (top), dots represent three microphone positions. Range of contour lines [−6; 6] Pa with increment 0.2 Pa.

In the shear layer at the nozzle radius of the jet (x/D = 0.5), strong pressure fluctuations develop due to strong vortices which are advected upwards and impact on the wall at $x/D \sim 0.5$ leading to large pressure fluctuations at the position of microphone 1 (black dot). The corresponding reconstructed pressure fields in a x-y-plane (showing the mirror-wall boundary condition) and at the wall in a x-z-plane are shown in Figure 11. Here, further outwards, following the flow in radial direction, the chain of alternating high- and low-pressure regions continues along the wall adjacent to microphone 2 and 3. The stagnation region with high pressure (maximum fluctuations reaching ~ 12 Pa) is a distinct feature in the pressure field.

The comparison of the two pressure time series in Figure 12 visualizes the agreement between microphone pressure and LPT pressure in a direct way. The pressure offset (black curve) is a small value and can be ruled out as a reason for the discrepancy between both signals. We obtain a high correlation coefficient of R = 0.88 for microphone 1. This value is among the highest reported in literature for pressure reconstruction from a turbulent boundary layer flow measurement. To some extent, the uncertainty of the reconstructed pressure field can be quantified based on the difference between both pressure data sets in Figure 12. The standard deviation of the difference signal is 0.36 Pa, 0.30 Pa, and 0.26 Pa, for microphone 1, 2 and 3. Assuming that the microphone recording has a negligible uncertainty, the magnitude of the difference signal can be interpreted as an uncertainty of the pressure field. This uncertainty of ~ 0.3 Pa is clearly higher than the value of ~ 0.1 Pa derived above from the uncertainty of the acceleration data. It seems that some uncertainty is added during the step of pressure reconstruction with FlowFit2. To validate the reconstruction strategy against the microphone

measurements, we compute the Pearson correlation coefficient $R = \langle P_1(t)P_2(t)\rangle/(\sigma_1\sigma_2)$ for the two time series, the pressure estimation from flow measurement $P_1(t)$ and the pressure recorded from the microphones $P_2(t)$ with their standard deviations σ_1 and σ_2 . Both pressure time series have first been filtered using a Butterworth filter with bandpass range [3, 150] Hz, the lower limit removing small frequencies and the upper limit corresponding to the low-pass cutoff frequency of the LPT trajectories when fit with a B-spline curve (TrackFit) (Gesemann et al. 2016). The microphone data have been down-sampled to the LPT frequency by linear interpolation. The high correlation coefficients $\langle R \rangle = 0.77$; $R_{max} = 0.88$) between the reconstructed pressure field and the microphone pressure signals show that the dominant pressure fluctuations of the flow can be reliably obtained from the LPT flow measurement even in such large volumes. At microphone position 2 and 3 the correlation values decrease mainly due to two reasons: First, the pressure fluctuation amplitudes induced by the vortical flow structures are reduced by dissipation in radial directions and thus at a given sensitivity of the STB + FlowFit2 pressure reconstruction system of around ~0.2 Pa the noise level increases. Second, the near wall boundary layer flow develops along the radial direction and here small-scale structures become dominant which are not well resolved by the present density of HFSB tracks. For a large measurement volume of 57 liters such a compromise leading to reduced correlation coefficients is a logical consequence.

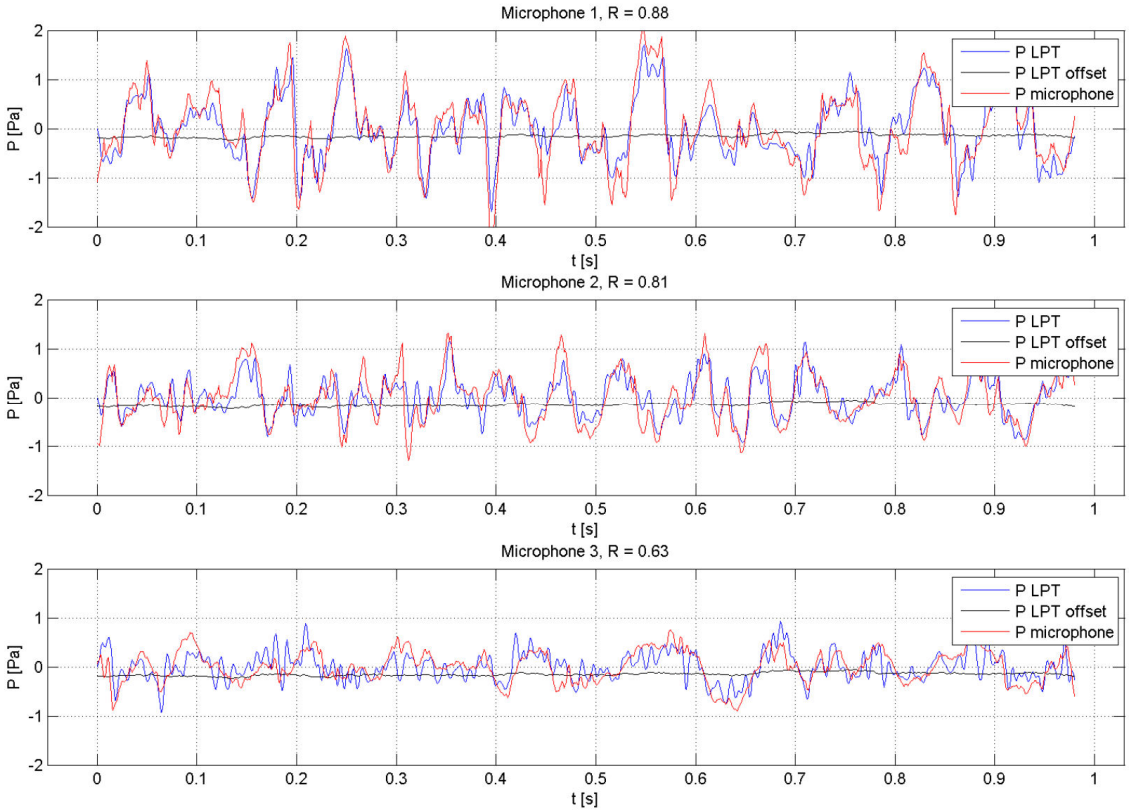

Figure 12: Direct comparison of pressure time series of the three microphones (red) and the reconstructed pressure from LPT (blue) at U = 4 m/s. The pressure offset is shown in black. Data is shown for the reconstruction with FlowFit2. Both pressure time series are bandpass filtered in the range [3; 150] Hz.

5.5 Conclusions on pressure from LPT data

In the presented measurement of Chapter 5, we are able to reconstruct the time-resolved 3D pressure field in a larger volume compared to previous pressure reconstructions (Ghaemi et al. 2012, Pröbsting et al. 2013, Schneiders et al. 2016) using HFSBs, pulsed LED illumination, high-speed cameras and Lagrangian particle tracking by STB. A local validation of the reconstructed pressure at critical points in the wall boundary layer shows that the dominant pressure fluctuations of the impinging jet (10 - 20 Hz) are well captured by the flow measurement. Smaller pressure fluctuations with higher temporal and spatial frequencies are less resolved at the chosen spatial and temporal resolution of the measurement; however, they are also less relevant for the estimation of integrated loads on the wall. The good agreement of the LPT pressure estimation based on the Navier-Stokes- constraint data assimilation approach FlowFit2 and the microphone pressure used as reference can be attributed to the accurate determination of the particle acceleration with STB, which has been shown to give better results than correlation-based PIV flow measurement techniques (see van Gent et al. 2017). The uncertainty of the measured acceleration is directly dependent on the position accuracy of tracked particles, which itself relies on the clear imaging of single particles. Using HFSB as large tracer particles has been shown to be suitable to image large measurement volumes (Huhn et al. 2017 Schanz et al. 2016b). Temporal and spatial resolution of the measurement limits the spectral range of pressure fluctuations that can be reconstructed. More details of the present study can be found in Huhn et al. 2018.

In conclusion, the use of highly seeded Lagrangian particle tracking with the Shake-The-Box (Schanz et al. 2016a) approach allows for the measurement of velocity and acceleration fields and the reconstruction of the time-resolved 3D pressure fields by FlowFit2 down to the wall of structures or models in a large volume. In low speed flows, unsteady pressure fluctuations in the order of ~ 0.5 Pa can be reliably measured, while the pressure sensitivity is scalable with the flow velocity and turbulence properties within the technical bounds of the imaging system. With such sensitivities, the method extends the accessible measurement range to small instantaneous pressure fluctuations that cannot be detected with pressure sensitive paint (PSP). Pressure reconstruction from dense Lagrangian particle tracking offers the possibility to derive small forces and moments on wings and models in the wind tunnel. It is therefore ideal for the study of unsteady flow phenomena and the induced loads on structures, e.g., for efficiency studies in biomimetic propulsion, Fluid-Strcuture-Interaction (FSI) or for the localization of the sources of aero-acoustic noise close to walls.

6 Upcoming 2nd LPT and DA Challenges

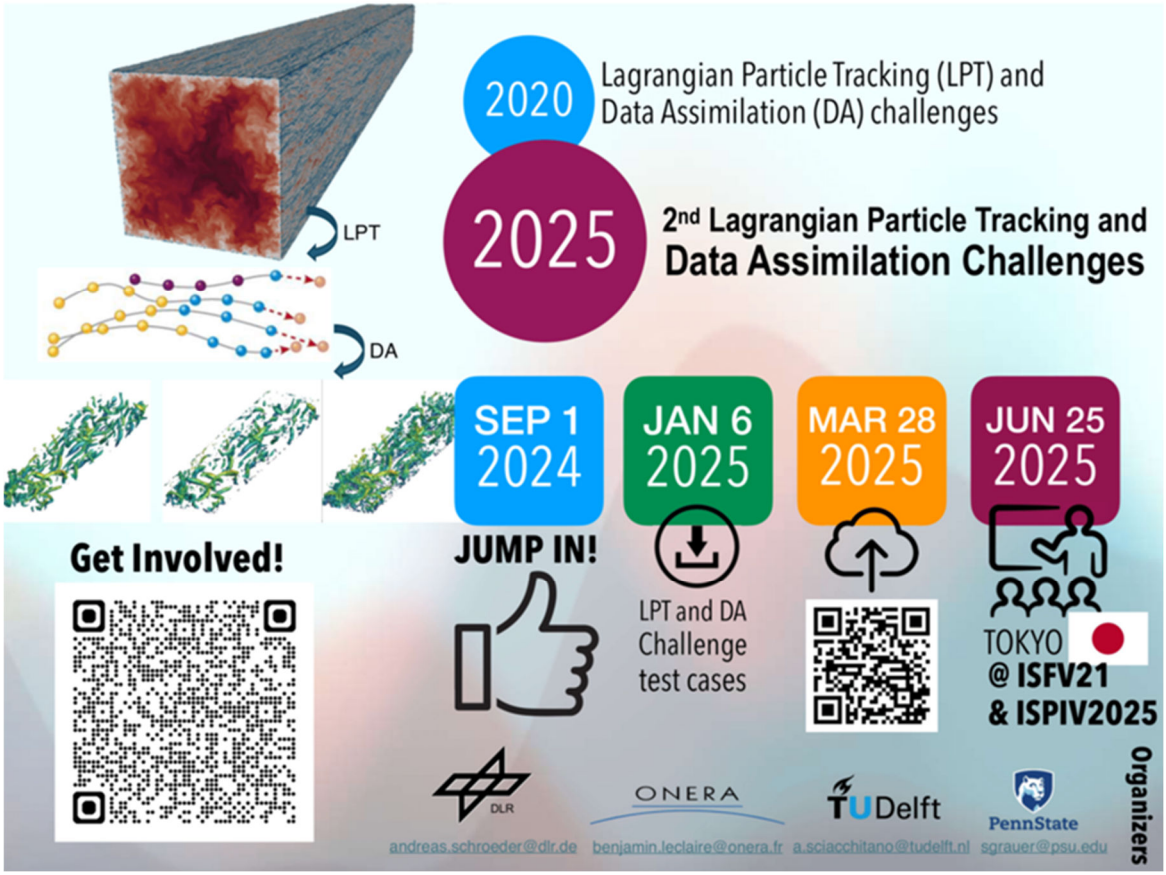

7 Acknowledgements

The authors would like to thank Janos Agocs, Stefan Haxter, Thomas Ahlefeldt, Dirk Michaelis, Uwe Dierksheide and Jiggar Shah for their help during the setup and execution of the experiment. We acknowledge the support of LaVision GmbH with camera equipment and the seeding generator. Work including the experimental results has partly been funded by the DFG-project *Analyse turbulenter Grenzschichten mit Druckgradient bei großen Reynoldszahlen mit hochauflösenden Vielkameramessverfahren* (grant KA 1808/14-1 and SCHR 1165/3-1).

This work was partly supported by the HOMER project from the European Union's Horizon 2020 research and innovation program under grant agreement No. 769237.

8 References

Agarwal K, Ram O, Wang J, Lu Y, Katz J (2021) Reconstructing velocity and pressure from noisy sparse particle tracks using constrained cost minimization. Exp Fluids 62:75

Agüera N, Cafiero G, Astarita T and Discetti S 2016 Ensemble 3D-PTV for high resolution turbulent statistics Meas. Sci. Technol. 27 124011

Agüí, J.C, & Jimenez, J. (1987), On the performance of particle tracking. ´ Journal of Fluid Mechanics185:447–468

Appelbaum J, Ohno D, Rist U, Wenzel C (2021) DNS of a turbulent boundary layer using inflow conditions derived from 4D-PTV data. Exp Fluids 62:1–21

Beneddine S, Yegavian R, Sipp D, Leclaire B (2017) Unsteady flow dynamics reconstruction from mean flow and point sensors: An experimental study. J Fluid Mech 824:174–201
Bhattacharya, S. & Vlachos, P.P. (2020), Volumetric particle tracking velocimetry (PTV) uncertainty quantification. Experiments in Fluids 61:1–18
Bogaert, I. (2014), Iteration-free computation of gauss–legendre quadrature nodes and weights. SIAM Journal on Scientific Computing 36:A1008–A1026
Bosbach J, Kühn M, Wagner C (2009) Large scale particle image velocimetry with helium filled soap bubbles. Exp Fluids 46:539–547
Bosbach, J., Schanz, D., Godbersen, P. & Schröder, A. (2021), Spatially and temporally resolved measurements of turbulent Rayleigh-Bénard convection by Lagrangian particle tracking of long-lived helium-filled soap bubbles, Proceedings of 14th International Symposium on Particle Image Velocimetry – ISPIV2021, August 1–4, 2021, Open Access https://ispiv21.library.iit.edu/, Doi:10.18409/ispiv.v1i1.208
Buchta DA, Zaki TA (2021) Observation-infused simulations of high-speed boundary-layer transition. J Fluid Mech 916:A44
Cai S, Mao Z, Wang Z, Yin M, Karniadakis GE. Physics-informed neural networks (PINNs) for fluid mechanics: A review. Acta Mechanica Sinica. 2021 Dec;37(12):1727-38
Cakir BO, Saiz GG, Sciacchitano A, van Oudheusden B (2022) Dense interpolations of LPT data in the presence of generic solid objects. Meas Sci Technol 33:124009
Chong, M. S., Perry, A. E. & Cantwell, B. J. (1990), A general classification of three-dimensional flow fields, Phys. Fluids A2(5), 765–777
Chakraborty P, Balachandar S & Adrian RJ (2005) On the relationships between local vortex identification schemes, J. Fluid Mech. 535:189-214
Chakraborty P, Balachandar S & Adrian RJ (2007) Kinematics of local vortex identification criteria. J. Visualization 10:137-140
Chandramouli P, Mémin E, Heitz D (2020) 4D large scale variational data assimilation of a turbulent flow with a dynamics error model. J Comput Phys 412:109446
Clark Di Leoni P, Agarwal K, Zaki TA, Meneveau C and Katz J (2023) Reconstructing turbulent velocity and pressure fields from under-resolved noisy particle tracks using physics-informed neural networks, Exp. Fluids 64:95
de Kat R, van Oudheusden BW (2012) Instantaneous planar pressure determination from PIV in turbulent flow. Exp Fluids 52:1089–1106
Discetti, S. & Coletti, F. (2018), Volumetric velocimetry for fluid flows, Meas. Sci. Tech. 29, 042001, 26 pp, Doi: 10.1088/1361-6501/aaa571
Discetti S, Liu Y (2022) Machine learning for flow field measurements: a perspective. Meas Sci Technol 34:021001
Du Y, Wang M, Zaki TA. State estimation in minimal turbulent channel flow: A comparative study of 4DVar and PINN. International Journal of Heat and Fluid Flow. 2023 Feb 1;99:109073.
Duraisamy K, Iaccarino G, Xiao H (2019) Turbulence modeling in the age of data. Annu Rev Fluid Mech 51:357–377
Ehlers F, Schröder A, Gesemann S (2020) Enforcing temporal consistency in physically constrained flow field reconstruction with FlowFit by use of virtual tracer particles. Meas Sci Technol 31:094013
Etebari A, Vlachos PP (2005) Improvements on the accuracy of derivative estimation from DPIV velocity measurements, Exp. Fluids 39:1040-1050
"Forced isotropic turbulence" data-set description from Johns Hopkins Turbulence Data Base http://turbulence.pha.jhu.edu/Forced_isotropic_turbulence.aspx
Fukami K, Fukagata K, Taira K (2021) Machine learning based spatio-temporal super resolution reconstruction of turbulent flows. J Fluid Mech 909:A9

Gesemann, S., Huhn, F., Schanz, D., & Schröder, A. (2016) From noisy particle tracks to velocity, acceleration and pressure fields using B-splines and penalties. 18th Int. Symp. on Appl. of Laser and Imaging Tech. to Fluid Mech. Lisbon, Portugal, July 4 – 7 2016

Gesemann, S.et al. (2021), Trackfit: Uncertainty quantification, optimal filtering and interpolation of tracks for time-resolved Lagrangian particle tracking. in 14th International Symposium on Particle Image Velocimetry

Ghaemi S, Ragni D, Scarano F (2012) PIV-Based pressure fluctuations in the turbulent boundary layer. Exp Fluids 53:1832–1840

Giordano, M. (2016), Uncertainty propagation with functionally correlated quantities. arXiv e-prints, arXiv:1610.08716

Godbersen, P. & Schröder, A. (2020), Functional binning: improving convergence of Eulerian statistics from Lagrangian particle tracking, Measurement Science and Technology, 31, 9, 095304, IOP Publishing

Godbersen, P. & Schröder, A. (2021), Enhanced functional binning for one- and two-point statistics using a posteriori Uncertainty Quantification of LPT data, Proceedings of 14th International Symposium on Particle Image Velocimetry – ISPIV2021, August 1–4, 2021, Doi:10.18409/ispiv.v1i1.126

Godbersen, P., Gesemann, S., Schanz, D. & Schröder, A. (2024), FlowFit3: Efficient data assimilation of LPT measurements, Paper 216, 21th International Symposium on Application of Laser and Imaging Techniques to Fluid Mechanics • LISBON | PORTUGAL • JULY 8-11, 2024

Gronskis A, Heitz D, Mémin E (2013) Inflow and initial conditions for direct numerical simulation based on adjoint data assimilation. J Comput Phys 242:480–497

Haller, G. (2015), Lagrangian Coherent Structures, Annu. Rev. Fluid Mech. 2015. 47:137–62, doi: 10.1146/annurev-fluid-010313-141322

Haller, G., Hadjighasem, A., Farazmand, M. & Huhn, F. (2016), Defining coherent vortices objectively from the vorticity, J. Fluid Mech 795:136-173.

Hammond, A. & Meng, H. (2021) Particle radial distribution function and relative velocity measurement in turbulence at small particle-pair separations. Journal of Fluid Mechanics 921:A16

Hanrahan S, Kozul M, Sandberg RD (2023) Studying turbulent flows with physics-informed neural networks and sparse data. Int J Heat Fluid Flow 104:109232

Harlow FH, Welch JE. (1965). Numerical Calculation of Time-Dependent Viscous Incompressible Flow of Fluid with Free Surface. The Physics of Fluids, 8(12), 2182-2189

He C, Wang P, Liu Y, Gan L (2022a) Flow enhancement of tomographic particle image velocimetry measurements using sequential data assimilation. Phys Fluids 34:035101

He C, Zeng X, Wang P, Wen X, Liu Y (2024) Four-dimensional variational data assimilation of a turbulent jet for super-temporal-resolution reconstruction. J Fluid Mech 978:A14

Huhn, F., Schanz, D., Gesemann, S., Dierksheide, U., van de Meerendonk, R., Schröder, A. (2017), Large-scale volumetric flow measurement in a pure thermal plume by dense tracking of helium-filled soap bubbles. Exp Fluids 58:116

Huhn, F., Schanz, D., Manovski, P., Gesemann, S. & Schröder, A. (2018), Time-resolved large-scale volumetric pressure fields of an impinging jet from dense Lagrangian particle tracking, Exp Fluids, 59, 5, 1-16

Jahn, T., Schanz, D. & Schröder, A. (2021), Advanced Iterative Particle Reconstruction for Lagrangian Particle Tracking, Experiments in Fluids 62 (8), 1-24, doi: 10.1007/s00348-021-03276-7

Jeon YJ, Earl T, Braud P, Chatellier L, David L (2015) 3D pressure field around an inclined airfoil by tomographic TR-PIV and its comparison with direct pressure measurements, 18th Int. Symp. on Applications of Laser Techniques to Fluid Mechanics, Lisbon, Portugal

Jeon YJ, Müller M, Michaelis D (2022) Fine scale reconstruction (VIC#) by implementing additional constraints and coarse-grid approximation into VIC+. Exp Fluids 63:70

Jeong, J. & Hussain, F. (1995), On the identification of a vortex, J. Fluid Mech.: 285, 69-94

Kähler, C. J., Scharnowski, S. & Cierpka, C. (2012), On the resolution limit of digital PIV, Exp In Fluids, 52, pp 1629-1639

Kähler, C. J., Astarita, T., Vlachos, P. P., Sakakibara, J., Hain, R., Discetti, S., La Foy, R. & Cierpka, C (2016), Main results of the 4th International PIV Challenge, Exp in Fluids, 57(6), 97

Kurtulus DF, Scarano F, David L (2007) Unsteady aerodynamic forces estimation on a square cylinder by TR-PIV, Exp. Fluids 42:185-196

Lemke M, Sesterhenn J (2016) Adjoint-based pressure determination from PIV data in compressible flows—validation and assessment based on synthetic data. EuR J Mech B-Fluid 58:29-38

Leoni PCD, Agarwal K, Zaki TA, Meneveau C, Katz J (2023) Reconstructing turbulent velocity and pressure fields from under-resolved noisy particle tracks using physics-informed neural networks. Exp Fluids 64:95

Li L, Pan Z (2024) Three-dimensional time-resolved Lagrangian flow field reconstruction based on constrained least squares and stable radial basis function. Exp Fluids 65:57

Li, Y., Perlman, E., Wan, M., Yang, Y., Burns, R., Meneveau, C., Burns, R., Chen, S., Szalay, A., Eyink, G. (2008), A public turbulence database cluster and applications to study Lagrangian evolution of velocity increments in turbulence. J. of Turb 9, No. 3.

Liu DC and Nocedal J. (1989) On the limited memory BFGS method for large scale optimization. Mathematical Programming, 45(1–3), 503–528.

Lourenco, L. & Krothapalli, A. (1995), On the accuracy of velocity and vorticity measurements with PIV, Exp. Fluids 18:421-428

Manovski, P., Novara, M., Mohan, N. K. D., Geisler, R., Schanz, D., Agocs, J., Godbersen, P. & Schröder, A. (2021), 3D Lagrangian particle tracking of a subsonic jet using multi-pulse Shake-The-Box, Experimental Thermal and Fluid Science, 123, 110346, 2021, Elsevier

Mogensen, P.K. & Riseth, A.N. (2018), Optim: A mathematical optimization package for Julia. Journal of Open Source Software 3:615

Mons V, Marquet O, Leclaire B, Cornic P, Champagnat F (2022) Dense velocity, pressure and Eulerian acceleration fields from single-instant scattered velocities through Navier–Stokes-based data assimilation. Meas Sci Technol 33:124004

Murai Y, Nakada T, Suzuki T, Yamamoto F (2007) Particle tracking velocimetry applied to estimate the pressure field around a Savonius turbine. Meas Sci Technol 18:2491–2503

Navon IM (2009) Data assimilation for numerical weather prediction: A review. In: Park, S.K., Xu, L. (eds) Data assimilation for atmospheric, oceanic and hydrologic applications. Springer Publishing Company, Incorporated, Springer, Berlin, Heidelberg

Novara, M. & Scarano, F. (2013), A particle-tracking approach for accurate material derivative measurements with tomographic PIV. Exp Fluids 54:158

Novara, M., Schanz, D., Reuther, N., Kähler, C. J. & Schröder, A. (2016), Lagrangian 3D particle tracking in high-speed flows: Shake-The-Box for multi-pulse systems, Exp. Fluids 57:128

Novara, M., Schanz, D., Gesemann, S., Lynch, K.P. & Schröder, A. (2016b), Lagrangian 3D particle tracking for multi-pulse systems: performance assessment and application of Shake-The-Box, 18th Lisbon Symposium, July 4-7, Lisbon, Portugal

Novara, M., Schanz, D., Geisler, R., Gesemann, S., Voss, C. & Schröder A (2019), Multi-exposed recordings for 3D Lagrangian particle tracking with multi-pulse Shake-The-Box. Experiments in Fluids, 60(3), 1-19

Ouellette, N.T., Xu, H. & Bodenschatz, E. (2006), A quantitative study of three-dimensional lagrangian particle tracking algorithms. Experiments in Fluids 40:301–313

Pope SB (2000), Turbulent Flows, Book, Cambridge University Press, ISBN 0521598869, 9780521598866

Pröbsting S, Scarano F, Bernardini M, Pirozolli S (2013) On the estimation of wall pressure coherence using time-resolved tomographic PIV. Exp Fluids 54:1567

Raffel, M., Willert, C. E., Scarano, F., Kähler, C. J., Wereley, S. T., & Kompenhans, J. (2018),. Particle image velocimetry: a practical guide. Springer.

Raiola, M., Lopez-Nunez, E., Cafiero, G. & Discetti S (2020), Adaptive ensemble PTV. ˜ Measurement Science and Technology 31:085301

Raissi M, Perdikaris P, Karniadakis GE (2019) Physics-informed neural networks: A deep learning framework for solving forward and inverse problems involving nonlinear partial differential equations. J Comput Phys 378:686–707

Raissi M, Yazdani A, Karniadakis GE (2020) Hidden fluid mechanics: learning velocity and pressure fields from flow visualizations. Science 367:1026-1030

Richardson, L. F. (1922), Weather Prediction by Numerical Process. Cambridge University Press

Rival D, van Oudheusden BW (2017) Load-estimation techniques for unsteady incompressible flows. Exp Fluids 58:20

Scarano, F. (2013), Tomographic PIV: principles and practice, Meas. Sci. Technol. 24 012001, Doi: 10.1088/0957-0233/24/1/012001/

Scarano F, Schneiders JFG, Saiz GG, Sciacchitano A (2022) Dense velocity reconstruction with VIC-based time-segment assimilation. Exp Fluids 63:96

Schanz, D., Schröder, A., Gesemann, S., Michaelis, D. & Wieneke, B. (2013), Shake-The-Box: a highly efficient and accurate Tomographic Particle Tracking Velocimetry (TOMO-PTV) method using prediction of particle position, 10th Symp. on PIV, Delft, The Netherlands

Schanz, D., Gesemann, S. & Schröder, A. (2016a), Shake-The-Box: Lagrangian particle tracking at high particle image densities. Exp. Fluids, 57(5), 1-27. Doi: 10.1007/s00348-016-2157-1

Schanz D, Huhn F, Gesemann S, Dierksheide U, van de Meerendonk R, Manovski P, Schröder A (2016b), Towards high-resolution 3D flow field measurements at cubic meter scales, *18th Int. Symp. on Applications of Laser Techniques to Fluid Mechanics*, Lisbon, Portugal

Schanz, D., Novara, M. & Schröder, A. (2021), Shake-The-Box particle tracking with variable time-steps in flows with high velocity range (VT-STB), Proceedings of 14th International Symposium on Particle Image Velocimetry – ISPIV2021, August 1–4, 2021, Doi:10.18409/ispiv.v1i1.65

Schneiders JFG, Caridi GCA, Sciacchitano A, Scarano F (2016) Large-scale volumetric pressure from tomographic PTV with HFSB tracers. Exp Fluids 57:164

Schneiders JFG, Pröbsting S, Dwight RP, van Oudheusden BW, Scarano F (2016a) Pressure estimation from single-snapshot tomographic PIV in a turbulent boundary layer. Exp Fluids 57:53

Schneiders, J.F.G. & Scarano, F. (2016b), Dense velocity reconstruction from tomographic PTV with material derivatives. Exp Fluids 57, 139 (2016). Doi:10.1007/s00348-016-2225-6

Schröder, A., Schanz, D., Michaelis, D., Cierpka, C., Scharnowski, S. & Kähler, C. J. (2015), Advances of PIV and 4D-PTV" Shake-The-Box" for turbulent flow analysis–the flow over periodic hills, "Flow, Turbulence and Combustion", 95, 2, 193-209, Springer Netherlands

Schröder, A. & Schanz, D. (2023), 3D Lagrangian Particle Tracking in Fluid Mechanics, Annu. Rev. Fluid Mech. 2023. Bd. 55:511–540, https://doi.org/10.1146/annurev-fluid-031822-041721

Sciacchitano A, Leclaire B and Schröder A (2021) Main results of the first Data Assimilation Challenge. In 14th International Symposium on Particle Image Velocimetry – ISPIV 2021, August 1–5, 2021

Sperotto P, Pieraccini S, Mendez MA (2022) A meshless method to compute pressure fields from image velocimetry. Meas Sci Technol 33:094005

Suzuki T, Ji H, Yamamoto F (2009a) Unsteady PTV velocity field past an airfoil solved with DNS: Part 1. Algorithm of hybrid simulation and hybrid velocity field at Re≈103. Exp Fluids 47:957–976

Suzuki T, Sanse A, Mizushima T, Yamamoto F (2009b) Unsteady PTV velocity field past an airfoil solved with DNS: Part 2. Validation and application at Reynolds numbers up to $Re \leq 10^4$. Exp Fluids 47:977–994

Suzuki T, Yamamoto F (2015) Hierarchy of hybrid unsteady-flow simulations integrating time-resolved PTV with DNS and their data-assimilation capabilities. Fluid Dyn Res 47:051407

Tronchin T, David L, Farcy A (2015), Loads and pressure evaluation of the flow around a flapping wing from instantaneous 3D velocity measurements. Exp Fluids 56:7

van Gent, P. L., Michaelis, D., van Oudheusden, B. W., Weiss, P.-É., De Kat, R., Laskari, A., Jeon, Y., David, L., Schanz, D., Huhn, F., Gesemann, S., Novara, M., McPhaden, C., Neeteson, N. J., Rival, D. E., Schneiders, J. F. G. & Schrijer, F. F. J. (2017), Comparative assessment of pressure field reconstructions from PIV measurements and Lagrangian particle tracking, Exp Fluids 58:33

van Oudheusden BW, Scarano F, Roosenboom EWM, Casimiri EWF, Souverein LJ (2007) Evaluation of integral forces and pressure fields from planar velocimetry data for incompressible and compressible flows, Exp. Fluids 43:152-162

van Oudheusden BW (2013) PIV-based pressure measurement, Meas. Sci. Technol. 24 032001

Wang M, Zaki TA (2021) State estimation in turbulent channel flow from limited observations. J Fluid Mech 917:1–29

Wieneke B (2008) Volume self-calibration for 3D particle image velocimetry. Exp Fluids 45:549–556

Wieneke B. (2013) Iterative reconstruction of volumetric particle distribution. Meas Sci Technol, 24 024008.

Willert C (2015) High-speed particle image velocimetry for the efficient measurement of turbulence statistics, Exp. Fluids 56:17, doi 10.1007/s00348-014-1892-4

Yeung PK, Donzis DA, Sreenivasan KR. (2012). Dissipation, enstrophy and pressure statistics in turbulence simulations at high Reynolds numbers. Journal of Fluid Mechanics, 700, 5–15.

Zauner M, Mons V, Marquet O, Leclaire B (2022) Nudging-based data assimilation of the turbulent flow around a square cylinder. J Fluid Mech 937:A38

Zhou K, Grauer SJ (2023) Flow reconstruction and particle characterization from inertial Lagrangian tracks. arXiv:2311.09076

Zhou K, Grauer S, Schanz D, Godbersen P, Schröder A, Rockstroh T, Jeon YJ, Wieneke B (2024). Benchmarking data assimilation algorithms for 3D Lagrangian particle tracking. In 21st International Symposium on the Application of Laser and Imaging Techniques to Fluid Mechanics, Lisbon, Portugal